HEPPA III intercomparison experiment on electron precipitation impacts, part I: Estimated ionization rates during a geomagnetic active period in April 2010

H. Nesse Tyssøy[1], M. Sinnhuber[2], T. Asikainen[3], S. Bender[4], M. A. Clilverd[5], B. Funke[6], M. van de Kamp[7], J. M. Pettit[8], C. E. Randall[8], T. Reddmann[2], C. J. Rodger[9], E. Rozanov[10,11], C. Smith-Johnsen[1], T. Sukhodolov[10,11], P. T. Verronen[3,7], J. M. Wissing[12], O. Yakovchuk[12,13,11]

[1]Birkeland Centre for Space Science, Department of Physics and Technology, University of Bergen, Norway
[2]Karlsruhe Institute of Technology, Hermann-von Helmholtz Platz 1, 76344 Leopoldshafen, Germany
[3]University of Oulu, Finland
[4]Birkeland Centre for Space Science, Norwegian University of Science and Technology, Trondheim, Norway
[5]British Antarctic Survey (UKRI-NERC), Cambridge, England
[6]Instituto de Astrofísica de Andalucía, CSIC, Granada, Spain
[7]Space and Earth Observation Centre, Finnish Meteorological Institute, Finland
[8]LASP, University of Colorado, Boulder, Colorado, USA
[9]University of Otago, New Zealand
[10]PMOD/WRC, Davos, Switzerland
[11]St. Petersburg State University, St. Petersburg, Russia
[12]University of Rostock, Germany
[13]Skobeltsyn Institute of Nuclear Physics, Lomonosov Moscow State University, Moscow, Russia

Key Points:

- Eight different electron ionization rates based on POES MEPED are compared.
- Differences of up to one order of magnitude between the highest and lowest ionization rates are found.
- The modeled response to the electron ionization rates varies by about a factor of eight in mesospheric NO density.

Corresponding author: Hilde Nesse Tyssøy, `hilde.nesse@uib.no`

Abstract

Precipitating auroral and radiation belt electrons are considered an important part of the natural forcing of the climate system. Recent studies suggest that this forcing is underestimated in current chemistry-climate models. The HEPPA III intercomparison experiment is a collective effort to address this point. Here, eight different estimates of medium energy electron (MEE) ($> 30\ keV$) ionization rates are assessed during a geomagnetic active period in April 2010. The objective is to understand the potential uncertainty related to the MEE energy input. The ionization rates are all based on the Medium Energy Proton and Electron Detector (MEPED) on board the NOAA/POES and EUMETSAT/MetOp spacecraft series. However, different data handling, ionization rate calculations, and background atmospheres result in a wide range of mesospheric electron ionization rates. Although the eight data sets agree well in terms of the temporal variability, they differ by about an order of magnitude in ionization rate strength both during geomagnetic quiet and disturbed periods. The largest spread is found in the aftermath of enhanced geomagnetic activity. Furthermore, governed by different energy limits, the atmospheric penetration depth varies, and some differences related to latitudinal coverage are also evident. The mesospheric NO densities simulated with the Whole Atmospheric Community Climate Model driven by highest and lowest ionization rates differ by more than a factor of eight. In a follow-up study, the atmospheric responses are simulated in four chemistry-climate models (CCM) and compared to satellite observations, considering both the CCM structure and the ionization forcing.

1 Introduction

The solar wind drives intrinsic magnetospheric processes responsible for accelerating and scattering particles into the middle atmosphere (the stratosphere, mesosphere, and lower thermosphere). The type of particle, the energy and the associated angle of incidence govern the ionization throughout the atmosphere. Auroral electrons (< 30 keV) and protons (< 1 MeV) from the plasmasheet deposit their energy in the lower thermosphere and upper mesosphere. Medium energy electrons (MEE) ($> 30\ keV$) from the radiation belts will ionize the upper mesosphere, whereas the high energy tail of MEE (> 300 keV) will reach even the upper stratosphere at auroral and sub-auroral latitudes (Turunen et al., 2009). On rare occasions the solar wind contains protons with sufficient energies (> 1 MeV) to impact the upper stratosphere directly over the entire polar cap.

Energetic particle precipitation (EPP) has long been known to impact the chemical composition of the upper atmosphere at high latitudes (Weeks et al., 1972; Swider & Keneshea, 1973; Crutzen et al., 1975). Over the last decades, spaceborne remote sensing abilities of trace gasses have enabled observations of EPP-produced reactive nitrogen (Sætre et al., 2004; Funke et al., 2014; Sinnhuber et al., 2016) and hydrogen species (Verronen et al., 2006; Andersson et al., 2012; Zawedde et al., 2016). Odd nitrogen has a lifetime of about one day in sunlit conditions in the lower thermosphere. In the polar winter darkness, however, it can exist for months, while being subject to both horizontal and vertical transport. The subsidence of odd nitrogen from its source region, the upper mesosphere and lower thermosphere, has been investigated (Randall et al., 2007; Bailey et al., 2014; Pérot et al., 2014; Funke et al., 2014; Hendrickx et al., 2015), along with the climate models' capability of reproducing it (Funke et al., 2017; Smith-Johnsen et al., 2018; Pettit et al., 2019; Arsenovic et al., 2019), and its impact on ozone concentration (Randall et al., 2005; Päivärinta et al., 2016; Andersson et al., 2018; Sinnhuber et al., 2018). In particular, the effects of the sporadic solar proton events (SPEs) have been extensively studied and are fairly well quantified (Jackman et al., 2005; Funke et al., 2011; Nesse Tyssøy & Stadsnes, 2015). Similarly, the link between energetic electron precipitation at auroral energies and NO in the lower thermosphere has been well established (Marsh et al., 2004; Sinnhuber et al., 2011). Knowledge gaps, however, remain regarding the frequency, intensity and the energy spectrum of the MEE precipitation, in particular in regard to high-energy tail, as well as their associated importance for atmospheric chemical changes.

The precipitating MEE can be detected for example via in-situ particle measurement or indirectly by observing the bremsstrahlung generated when the electrons decelerate in the atmosphere. While bremsstrahlung measurements up to now have mostly been point observations made during balloon campaigns (Millan et al., 2013; Mironova et al., 2019), satellite-borne particle measurements pass over the entire MEE precipitation region. For example the NOAA and MetOp POES series offer long, near continuous measurements dating back to 1979. During the latest decades a constellation of up to six operating satellites covering several magnetic local times has allowed for a more global perspective.

The Medium Energy Proton and Electron Detectors (MEPED) on board these spacecrafts have two telescopes pointing within, and close to the edge of, the bounce loss cone (BLC) (Rodger et al., 2010b). This makes MEPED one of few operating detectors that observes the particles that are lost to the atmosphere. The MEPED detector, however, suffers from several documented instrumental challenges, such as radiation damage (Galand & Evans, 2000; Asikainen & Mursula, 2011; Sandanger et al., 2015), cross-contamination (Evans & Greer, 2004; Yando et al., 2011) and non-ideal, energy dependent detection efficiency (Yando et al., 2011; Asikainen & Mursula, 2013). A number of different methods to account for the spurious response to protons in the electron detectors have been suggested (Lam et al., 2010; Peck et al., 2015; Nesse Tyssøy et al., 2016), along with estimates that assess the degradation of the solid state detectors (Asikainen & Mursula, 2011; Asikainen et al., 2012; Sandanger et al., 2015; Ødegaard et al., 2016). Further, several measures to account for the full loss cone have been suggested (Rodger et al., 2013; Peck et al., 2015; Asikainen & Ruopsa, 2016; Nesse Tyssøy et al., 2016). In addition, different choices are applied to create global maps of the MEE precipitation, as well as the shape of the energy spectrum (van de Kamp et al., 2016). There exist different methods of calculating the energy deposition throughout the atmosphere. The resulting ionization rate profiles will depend on the the background atmosphere itself. Consequently, despite the fact that most estimates of the MEE flux are based on the same fundamental set of observations, the electron ionization rates may differ considerably from each other.

For the first time, the Coupled Model Inter-comparison Project Phase 6 (CMIP6) includes MEE ionization as part of its solar forcing recommendation (Matthes et al., 2017). The MEE ionization rate data-set therein is based on the POES MEPED observations, and it uses the geomagnetic Ap index as a proxy to provide an extended time series beyond the satellite observation period (van de Kamp et al., 2016). There is, however, an ongoing debate to what extent this approach gives a representative flux level (Mironova et al., 2019; Nesse Tyssøy et al., 2019; Pettit et al., 2019; Clilverd et al., 2020). The discrepancies between the different ionization rate estimates might to a large extent be attributed to the different choices made in dealing with the instrumental challenges.

The High Energy Particle Precipitation in the Atmosphere (HEPPA) intercomparison experiments are designed to advance the EPP research with community-wide, collective efforts. While the HEPPA I experiment assessed the atmospheric impact of the Halloween 2003 solar proton event (Funke et al., 2011), and HEPPA II focused on the 2009 wintertime transport of EPP-NO_x (Funke et al., 2017), HEPPA III aims to improve the representation of MEE in atmosphere and climate models. The current study is the first of two papers to evaluate the MEE impact on the atmosphere from the multiple varying ionization rate databases. The main purpose of Part 1 is to give an overview of the available ionization rates and their different properties, in order to understand the uncertainty in the associated MEE impact on the atmosphere. An in-depth intercomparison of the MEE response in different atmospheric models is provided by the companion paper (Sinnhuber et al., 2021).

Part 1 is organized as follows, Section 2 presents a review of eight different MEE ionization rate data sets. Section 3 compares the ionization rates during an event in April 2010 where the MEE precipitation is a prominent feature. The total hemispheric impact based on the eight ionization rates is compared, along with the temporal and spatial evolution seen at different pressure levels. Finally, in Section 4, the two data sets providing the highest and lowest ionization rates are applied in the Whole Atmosphere Community Climate Model (WACCM), and the associated impact on upper atmospheric chemistry is discussed.

2 Ionization rate estimates

To determine the MEE impact on the atmosphere, the energy deposition or ionization rate profile needs to be calculated. The derived energy deposition by MEE is dependent on: 1) the reconstruction of the global distribution of precipitating electron fluxes, 2) the method for calculating ionization rates, and 3) the background atmosphere in which the electrons propagate. In the following a short description of 1)-3) is given, after which eight different ionization rate estimates are presented: AIMOS, AISstorm, ApEEP, ISSI-19, FRES, OULU, MP15, and BCSS-LC.

1) Reconstruction of the global distribution of precipitating electron fluxes: The different MEE ionization rates are all based on electron fluxes measured by MEPED on board NOAA/POES and EUMETSAT/MetOp satellites. The satellites are Sun-synchronous, low-altitude ($\sim$ 850 km), polar orbiting spacecrafts. Their orbital period is about 100 min, resulting in 14–15 orbits each day. The NOAA and the MetOp satellite data sets together cover more than three solar cycles, with the first spacecraft NOAA-0 (TIROS-N) launched in 1978. The satellites from NOAA-0 up to NOAA-14 carried the first version of the instrument package, SEM (Space Environment Monitor)-1, which varies somewhat in instrumental construction and energy bands from the newer SEM-2. In the current paper we focus on the SEM-2 instrument package used on all spacecraft from NOAA-15 (launched in 1998) until MetOp-3 (launched in 2018). Here, we target a geomagnetically active period in April 2010 with six operating spacecraft traversing different magnetic local times as illustrated in Figure 1.

The SEM package consists of the Total Energy Detector (TED) and MEPED. TED is designed to measure the energy flux carried by auroral electrons and protons according to electron band 4 to 14 (154 eV–9.5 keV), and additionally provides information on the energy spectrum and characteristic energy of the measured particles (Evans & Greer, 2004). The MEPED instrument consists of two directional electron telescopes and two directional proton telescopes, as well as an omni-directional detector for very energetic protons measured over a wide range of angles (Evans & Greer, 2004). The nominal energy limits of the MEPED telescopes cover the energy range of MEE as listed in Table 1. The actual response of the MEPED telescope to the electrons as well as proton contamination is quite complex (see for example Yando et al. (2011)).

The two MEPED electron and proton telescopes are mounted perpendicular to each other, and are referred to as the 0° detector and the 90° detector. The 0° detector points radially out from Earth, and can, at high latitudes, detect particle fluxes at small pitch angles near the center of the loss cone. At high geomagnetic latitudes ($>\sim 50^\circ N/S$) the 90° detectors measure the trapped particle population near the edge of the loss cone. At satellite altitude the size of the loss cone varies from $\sim$56° to $\sim$65° over L shell 2–10. The pointing direction of the 0° and 90° telescopes vary from 0° to $\sim$40° and $\sim$58° to $\sim$125° over the same interval, respectively (Nesse Tyssøy et al., 2019). A detailed discussion on what radiation belt populations the 0° and 90° telescopes measure, and how this varies for differing locations around the Earth, has been presented in Appendix A in Rodger et al. (2010a). The field of view of both the 0° and 90° telescopes is 30° full width.

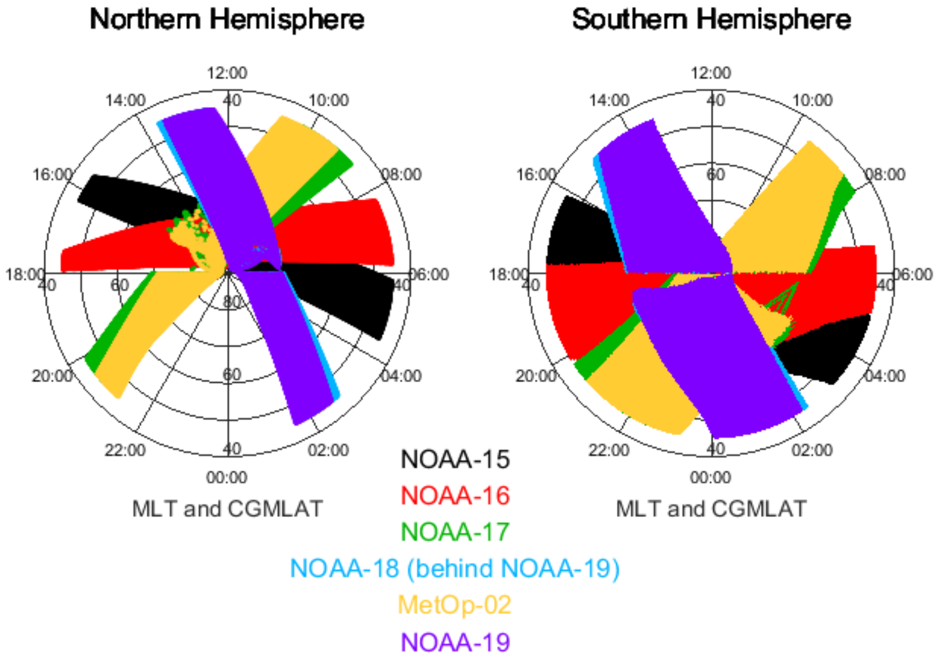

Figure 1: The magnetic local time coverage of the NOAA/POES and EUMETSAT/MetOp series in April 2010.

Channel	Nominal Energy Range	Sensitive to protons having energies
E1	> 30 keV	210 keV - 2700 keV
E2	> 100 keV	280 keV - 2700 keV
E3	> 300 keV	440 keV - 2700 keV
P6	—	> 6900 keV

Table 1: Nominal MEPED Electron Energy Range and sensitivity to proton contamination (Evans & Greer, 2004)

Despite MEPED being a common starting point, the fluxes used in the eight ionization rate estimates differ in several ways. For example, the different estimates use different approaches to remove the contamination of protons from the electron measurements, some considering also the proton instrument degradation. Some of the estimates consider non-ideal, energy dependent electron detector sensitivity, the effects of which can be expressed by using effective energy ranges slightly differing from those in Table 1. Further, the choice to use only the 0° detector data, or combine data from both the 0° and 90° detectors, is what sets the routines apart. Finally, the creation of a global map and choice of energy spectra impact the determination of the total amount of MEE precipitating into the atmosphere. Together, this leads to a wide variety of approaches to process and analyse the same initial MEPED observations.

2) The methods for calculating ionization rates: The ionization rate methods applied in this study can be divided into three broad categories: continuous loss methods, equation of transfer methods, and Monte Carlo simulations (Solomon, 2001). The continuous loss method uses a normalized energy dissipation distribution function for electrons (Rees, 1989). The majority of the eight ionization rate estimates apply the equation of transfer method, where the electron flux intensity in the atmosphere is calculated solving the steady state Boltzmann transport equations as functions of energy, pitch angle, and altitude. The ionization rate can then be derived with the knowledge of the flux intensity and the corresponding cross sections (Fang et al., 2008, 2010). In the Monte Carlo simulations the individual particles are discretized, making a probability estimate (Wissing & Kallenrode, 2009). All of the ionization rate estimates presented here assume an energy deposition of 35 eV per ionization. This is based on laboratory experiments where the energy per ionization is found to be 33 eV and 37 eV for O_2 and N_2, respectively. It is further assumed that it requires the same amount of energy to ionize O and O_2(Rees, 1989).

3) The background atmospheres: The medium in which the electron fluxes propagate will impact the ionization rate intensity and range. A real atmosphere is a dynamic medium which changes with season, latitude and local time. The simplest atmospheric model is a set of tables of air pressures, altitudes and temperatures as an average representation for all times and activity levels, such as e.g. the COSPAR International Reference Atmosphere (CIRA). Another empirical model, commonly used for Space physics applications, is the US Naval Research Laboratory - Mass Spectrometer and Incoherent Scatter radar model NRLMSIS (Picone et al., 2002). It includes variations due to solar cycle, season, time of day, latitude, as well as activity indices such as daily solar flux (F10.7) and geomagnetic activity (Ap). Full chemical-dynamical atmospheric models can also be applied, e.g. WACCM, HAMMONIA, EMAC, KASIMA etc. (see the companion paper Sinnhuber et al. (2021)). These can be used to provide the atmosphere for ionization rate calculations, or the ionization rates can be calculated self-consistently within the atmospheric model where the model itself will respond to e.g. increased Joule heating due to the calculated ionization rates or enhanced radiative cooling due to NO formation.

In the following subsections the eight different data ionization rate data-sets are described, where the differences and similarities are highlighted. Table 2 gives a short data handling summary. Figure 2 shows the approximate altitude and pressure range of the electron ionisation rate data-sets.

2.1 AIMOS

The Atmospheric Ionization Module Osnabrück (AIMOS) version 1.6 provides fluxes and ionization rates for electron energies from 0.154 to 300 keV with a 2-hour resolution (Wissing & Kallenrode, 2009).

The electron flux measurements are based on the 0° detectors from both TED and MEPED. The nominal integral channels of MEPED are converted into differential channels by subtracting the higher channels from the lower ones accounting for the width of the energy band, resulting in the bands 30-100 keV and 100-300 keV. To avoid cross-contamination, the electron fluxes are neglected when the high energy proton channel P7 detects more than 2 counts/s (1 count corresponds to about 100 $cm^2 sr$). This implies that measurements from the South Atlantic Anomaly (SAA) and during strong SPEs are effectively ignored.

Mean flux maps with a 3.6° geographic latitude and longitude resolution are calculated based on all 8 years of satellite data from 2002 to 2009. The maps are sorted by Kp level and four magnetic local time sectors. The upper and lower 25 % of the data have been neglected in order to reduce noise and outliers, while preserving the spatial pattern. The mean flux maps are scaled for every 2-hour time interval by real time data

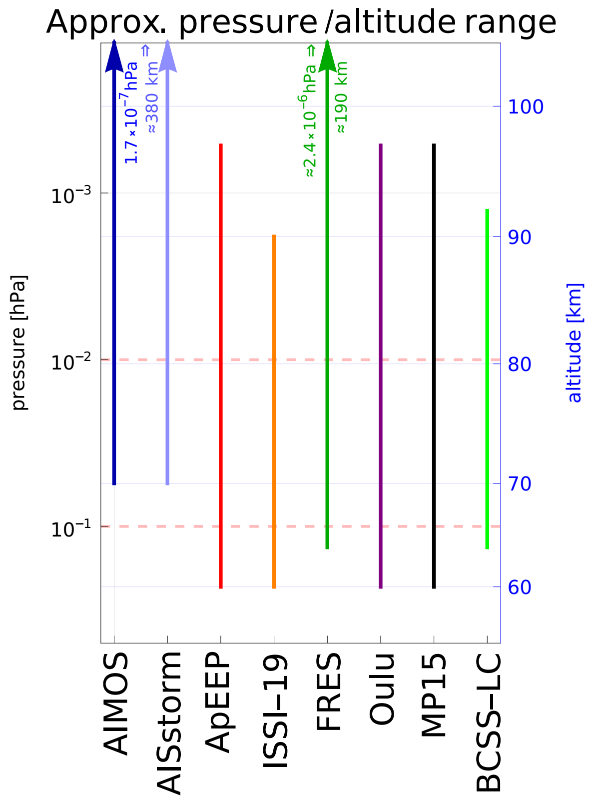

Figure 2: Approximate model specific altitude and pressure range of the electron ionization rates as determined from the energy range. Results are based on Monte-Carlo simulation using the Geant4 toolkit and the HAMMONIA atmosphere (April, 80°N, solmax (235 sfu)). The dashed lines indicate the pressure levels (0.01 hPa and 0.1 hPa) that have been chosen for a detailed inter-comparison in Sections 3.2 and 3.3. Note that the second pressure level is not covered by all models.

from two of the most recent NOAA and/or MetOp satellites. The scaling is limited to the regions of high fluxes to reduce the impact of noise in the real time data.

In order to reduce computing time, not every latitude and longitude bin is processed on its own. Instead, groups of bins with similar energy flux spectra have been determined manually. Each hemisphere is divided into one polar cap, and an auroral zone divided into 5 latitude bands with 4 magnetic local times each. For both hemispheres, this sums up to $(1 + (4 \times 5)) \times 2 = 42$ zones for every 2 h time step.

To move from individual flux channels to a continuous energy spectrum, the differential electron fluxes are fitted by up to five separate segments of power-law functions covering both the TED and MEPED energy bands. From this, the ionization rate is retrieved from a Monte-Carlo simulation with an energy resolution of 40 mono-energetic electron beams, equidistant in log-space on each magnitude, in an atmospheric detector using the GEANT 4 toolkit (Agostinelli et al., 2003). To account for the angular distribution of the incident electrons, 37 directions of incidence with respect to the vertical are considered. The Monte-Carlo simulation also accounts for ionization due to bremsstrahlung.

The background atmosphere in AIMOS is based on HAMMONIA (Schmidt et al., 2006) and the NRLMSISE-00 Model (Picone et al., 2002). HAMMONIA extends from the ground up to $1.7{\times}10^{-5}$ Pa, which corresponds to an upper boundary between 250 to 400 km depending on season, latitude and solar activity. All mono-energetic beams have been calculated for the latitudes 80°S, 60°S, 60°N, and 80°N, four seasons and three levels of solar activity (F10.7). For each calculated time interval, the most representative atmosphere is selected.

2.2 AISstorm

The Atmospheric Ionization during Substorm Activity, AISstorm, is a direct successor of AIMOS. The treatment of the electron fluxes is identical to AIMOS, with the same energy range (0.154–300 keV). However, both the time resolution (0.5 hour) and spatial resolution has been improved.

In AISstorm the grid is based on the modified 110 km altitude APEX (magnetic) coordinates (Richmond, 1995). The grid resolution is flexible, for common Kp levels it is 1° latitude and 15 min MLT (equivalent to 3.75° longitude). During rare, high Kp levels, the resolution may drop to 2° latitude vs. 1h MLT (= 15° longitude). The mean flux maps are based on 18 years (2001–2018) and sorted by Kp level and substorm condition. Missing data in these maps are substituted by weighted linear regression along MLT (or magnetic longitude). The flux maps are scaled by real time data from all available NOAA/MetOp satellites in the corresponding 30 min time step. The scaling method only takes into account areas where the flux maps and recent measurements are above average. This results in a set of preliminary scaling factors, one for each measurement. The final scaling factor is found by taking the median of all inter-comparisons. With this technique, the effect of outliers is significantly reduced and the numbers are most accurate for high flux values. After the scaling, every grid bin is processed further in contrast to AIMOS which combines similar precipitation zones. Apart from that, the method for converting the electron fluxes into ionization rate profiles is identical as for AIMOS.

2.3 ApEEP

The ApEEP model provides daily fluxes and ionization rates of MEE for the energy range 30 keV–1 MeV parametrized by the Ap index as described in van de Kamp et al. (2016).

The ApEEP model is based on MEPED observations from the 0° detector flux data acquired in the period 2002–2012. The electron flux data are corrected for low energy proton contamination (210–2700 keV) by estimating a series of piecewise exponential functions across the proton energy channels P2-P4, using a bow tie method to optimize the fit. The nominal contaminating energy ranges (Evans & Greer, 2004; Yando et al., 2011) are listed in Table 1. The integrated proton flux from 210–2700 keV, 280–2700 keV, and 440–2700 keV are then subtracted from the >30, >100 and >300 keV electron flux, respectively (Lam et al., 2010). In the case of high energy proton fluxes where the MEPED omni detector P7 (>36 MeV) detects more than 3 counts/s, the electron flux data are neglected. Similar to the AIMOS model, this effectively removes electron fluxes measured during large SPEs and associated with the SAA (Rodger et al., 2013). Further, to reduce noise contamination due to the relatively low sensitivity of the electron telescopes, all data points where the electron flux >30 keV was lower than 250 (s sr cm^2)$^{-1}$ are set to zero in all channels.

The electron flux data are binned with respect to their L-shell value (where L is the McIlwain L-parameter (McIlwain, 1961)) with a resolution of 0.5 for $L = 2$ to 10, and for every day. There is no distinction between different MLT sectors in the basic ApEEP model, although a follow-on study used improved data processing and provided an option of MLT-dependent electron fluxes (van de Kamp et al., 2018).

The averaged fluxes from all three energy channels are used to fit a power law spectral function for each day and L bin. This results in a value for the spectral gradient and the >30 keV flux for each day and L bin. These data are further binned according to Ap values, where the median in each bin is calculated to represent the most representative flux and spectral component. Finally, analytical expressions are fitted to the median values as functions of Ap and L-value (van de Kamp et al., 2016). In this, the dependence on L is expressed as the distance from the plasmapause, a dynamic boundary governing different radiation belt loss processes (Whittaker et al., 2014). For the location of the plasmapause, the model by O'Brien and Moldwin (2003) is used.

The atmospheric ionization is calculated on 168 logarithmically spaced energy bins from 30 keV to 1 MeV using the parameterization of electron impact ionization by Fang et al. (2010) where the background atmosphere is represented by the NRLMSISE-00 model (Picone et al., 2002). Fang et al. (2010) does not account for ionization due to bremsstrahlung. The ApEEP ionization rates are included in the CMIP6 solar forcing recommendation v3.2 (Matthes et al., 2017).

2.4 ISSI-19

The ISSI-19 data set offers daily resolved MEE ionization rates starting in 1998. It is comparable to those presented earlier by Orsolini et al. (2018) and Newnham et al. (2018), who used an earlier version with similar data handling (ISSI-14). It covers the electron energy range from 30 keV to 1 MeV.

ISSI-19 is based on the MEPED 0° detector flux measurements. It applies the same low energy proton flux corrections and noise level criteria as the ApEEP parameterization. All operational POES measurements are zonally averaged in geomagnetic coordinates with 3-hr time resolution and 0.5 L resolution. The data are restricted to the L range from 2.25 to 9.75, which encompasses the outer radiation belt. An electron spectrum is derived by fitting a differential power law flux spectrum covering the energy range from 30 keV to 1 MeV. The power law assumption and the energy range for the spectrum is the same as the one applied in the ApEEP ionization rate routine (van de Kamp et al., 2016), described in the previous paragraph. The main difference compared to ApEEP is that the resulting ISSI-19 flux data were not further parametrized as functions of Ap and L, but used as such. As a result of this, ISSI-19 is only suitable to investigate time periods covered by POES MEPED SEM-2 observations (currently spanning 1998-2019, with caveats), while ApEEP was created for much longer climate modelling runs outside the era of satellite data.

The method of calculating the ionization rate is the same as for the ApEEP routine, it uses the method of Fang et al. (2010) and the atmospheric composition from the NRLMSISE-00 model.

This model is named ISSI-19 as the fundamental processing approach was developed at the International Space Science Institute (ISSI) by an ISSI International Team in April–May 2014. The ISSI-19 model builds on the earlier ISSI-14 approach for processing MEPED measurements (including all SEM-2 data from all NOAA and MetOp spacecraft), it was updated during discussions at the CHAMOS (Chemical Aeronomy in the Mesosphere and Ozone in the Stratosphere) EEP meeting in Helsinki in April 2019. ISSI-type rates were first published by Orsolini et al. (2018). The appendix of that publication provides a description of the spectrum and ionization calculations, which are common to both the ISSI-14 and ISSI-19 models. The primary differences in the MEPED data processing between ISSI-14 and ISSI-19 come from improvements in our understanding of low-Earth orbit electron flux measurements, changes that allow more modern spacecraft data to be ingested in the data set (including allowing for format changes) (Whittaker et al., 2013), and also corrections in the code that performs the proton contamination correction (Whittaker et al., 2014).

2.5 FRES

The Full Range Energy Spectrum (FRES) provides fluxes and ionization rates of MEE for the energy range 1-750 keV with a 3-hour resolution (Smith-Johnsen et al., 2017).

The FRES model is based on the 0° detector flux measured by both TED and MEPED (similar to the AIMOS and AISSTORM model). It diverts from the nominal energy resolution given in Table 1. The detector efficiency depends on the incoming energy. Ødegaard et al. (2017) determine an optimized effective integral energy limit and associated geometric factors assuming both power law and exponential spectra to give a reasonable representation of the incoming electron energies. The new, optimized energy limits applied are > 43, > 114, and > 292 keV.

Low energy proton contamination is accounted for, but as opposed to the ApEEP model and the ISSI-19 dataset, it first applies a correction to the energy ranges of the proton channels. The solid state proton detectors degrade over time as a result of radiation damage (Galand & Evans, 2000; Asikainen & Mursula, 2011; Asikainen et al., 2012; Sandanger et al., 2015). This impact becomes significant after 2–3 years of operation, changing the energy ranges of the proton detector. The increasing proton detector energy limits are taken into account in a quantitative assessment of the data (Sandanger et al., 2015; Ødegaard et al., 2016). Subsequently, a monotonic Piecewise Cubic Hermite Interpolating Polynomial (PCHIP) is applied to the corrected proton fluxes, and the proton flux in the energy ranges known to impact the respective electron channels (see Table 1) are then retrieved and subtracted from the original measured electron fluxes.

Higher-energy electrons are also a source of contamination in the proton detector channels P1, P2, P3, or P6, while P4 and P5 have low sensitivity to relativistic electrons (Yando et al., 2011). Hence, in the absence of protons in the P5 channel, the count rate in the proton channel P6 is registered as > 756 keV electron fluxes (Nesse Tyssøy et al., 2016; Ødegaard et al., 2017).

All available NOAA and EUMETSAT passes are utilized. Every 3-hour the flux values in each energy channel are interpolated in corrected geomagnetic coordinates and then converted to geographical coordinates of 4° latitude and 10° longitude. To construct a continuous energy spectrum, the highest three TED channels (0.688–1.000 keV, 2.115–3.075 keV, and 6.503–9.457 keV) are fitted to an exponential or a Maxwellian spectrum depending on the ratio between the first two channels: if channel 1 is higher than channel 2, an exponential fit is used, and if channel 2 is highest, a Maxwellian fit is used. MEPED's integral channels are converted into differential channels resulting in the bands 43-114 keV, 114-292 keV, and 292-756 keV applying a power law fit.

The FRES model applies the continuous loss method by Rees (1989). It does not account for ionzation due to bremsstrahlung. The atmospheric parameters are retrieved from the standard reference atmosphere (Committee on Space Research International Reference Atmosphere 1986). Hence, the reference atmosphere does not vary with season, latitude, or solar activity.

2.6 OULU

The University of Oulu has constructed a corrected electron flux data set of MEPED observations from all POES satellites including the satellites carrying the SEM-1 (satellites launched before 1998) and SEM-2 (satellites launched after 1998) detector suites. It provides daily MEE fluxes and ionization rates in the energy range 30 keV - 1 MeV.

The Oulu flux data set incorporates instrumental corrections for proton detector degradation due to radiation damage (Asikainen & Mursula, 2011; Asikainen et al., 2012). For electron observations the data set considers the energy dependent instrument sensitivity and, similarly as the FRES routine, removes contamination due to protons after taking into account how the proton detectors degrade over time (Asikainen & Mursula, 2013).[1]

The latitude distribution is computed separately for both hemispheres in corrected geomagnetic latitude with a resolution of 2°, and the fluxes correspond to averages from two opposite MLT sectors (dawn 7 MLT and dusk 19 MLT), which are close to the overall zonal average over all MLT sectors (Asikainen & Ruopsa, 2019).

The Oulu routine incorporates measurements from both the 0° and 90° MEPED telescopes to estimate the precipitating fluxes. It uses an average of the logarithmic 0° and 90° telescope fluxes (F_0 and F_{90}) according to

$$\log_{10} F_{prec} = \frac{1}{2} \left(\log_{10} F_0 + \log_{10} F_{90} \right). \tag{1}$$

This is a very rough approximation for the precipitating flux and likely less accurate than the approach employed, e.g., by the BCSS-LC dataset described below. However, the simplistic choice for F_{prec} can be justified by considering an often used approximation for the particle pitch angle distribution, which is of form

$$J(\alpha_{sat}) = A \sin^n(\alpha_{sat}), \tag{2}$$

where A and n are positive constants and J is the flux (1/cm^2 sr s) as a function of pitch angle α_{sat} at the satellite. Knowing the central pitch angles of the particles entering the MEPED telescopes, and integrating Equation 2 over the field of view of both telescopes, one can find values of A and n which best fit each momentary pair of F_0 and F_{90} observations. As a more refined approximation to the total precipitating flux F_{prec}, one can then integrate the obtained pitch angle distribution over the solid angle corresponding to the pitch angle range from 0° to the local BLC width angle α_{BLC}, which is easily determined from equation

$$\sin(\alpha_{BLC}) = \sqrt{\frac{B_{sat}}{B_0}}, \tag{3}$$

where B_{sat} is the magnetic field strength at the satellite location and B_0 is the magnetic field strength at 120 km altitude at the foot-of-the field line threading the satellite location. Such a calculational exercise (though not shown here in detail) indicates that F_{prec} obtained by Eq. 1 is rather close on average to the more sophisticated estimate of Equation 1, for all values of A and n typically observed in the data.

The daily average latitude distributions of the electron fluxes are equally spread zonally to all longitudes thereby yielding a zonally symmetric flux distribution. The integral energy spectrum of electrons is first estimated by fitting piece-wise power-law spectra to the three energy channels. The integral fluxes from 30 keV to 1 MeV, are then retrieved from this fit with a 10 keV step size. The corresponding differential spectrum is numerically estimated by differentiating the integral spectrum. The subsequent ionization rate calculation is similar to the ApEEP and ISSI-19 routines, applying the Fang et al. (2010) parameterization. The background atmosphere is represented by the NRLMSISE-00 model (Picone et al., 2002).

[1] Additional corrections to the SEM-1 data: Corrections to account for electronic noise in the detector chips is applied. The data set also fixes some errors in the satellite position in the SEM-1 data and incorporates a set of fully recalculated auxiliary data dependent on satellite position (e.g., spacecraft coordinates in different systems, L-values, MLTs, telescope pitch angles etc.) (Asikainen, 2017).The composite adjusts the instrumentally corrected observations further for cosmic ray related background noise, slowly changing satellite location and for the differences between SEM-1 and SEM-2 telescope viewing directions. This full corrected dataset of all POES satellites was recently used to produce a homogenized long-term composite record of daily averaged latitude distribution of electron fluxes from the three electron energy channels from 1979 to present (Asikainen & Ruopsa, 2019; Asikainen, 2019).

2.7 MP15

The MP15 routine provides daily electron fluxes and ionization rates for the energy range 27 keV-1 MeV (Peck et al., 2015; Pettit et al., 2019).

Low-energy proton contamination is accounted for by utilizing the estimated geometric factors by Yando et al. (2011) and the inversion methods described in (Peck, 2014). The proton differential spectrum is derived by fitting a combined spectrum of relativistic Maxwellian, double Maxwellian, power law, and exponential form to the differential proton energy channels, P1-P5. Next, a forward model calculates the total proton contamination in the electron channels, after which the data from the electron channels are put through the inversion method to calculate the corrected electron differential fluxes (Peck et al., 2015).

Similar to the FRES routine, the MP15 uses the P6 channel as an additional electron channel. The proton spectra, fitted onto P1-P5, are extrapolated to higher energies. The discrepancies between the extrapolated fits and the fluxes measured in P6 are then assumed to be primarily due to electrons > 700 keV.

Like the Oulu routine, the MP15 routine utilizes fluxes from both the 0° and 90° telescopes to create an estimate of the precipitating fluxes. The pitch angle (α) dependence of the precipitating particle flux is assumed to vary as a sine function shown in Equation 2, where 'n' is assumed to be 1 for the sake of simplicity. A is determined based on the 0° and 90° fluxes and the pointing directions of the telescopes. Similarly as in the Oulu routine, the BLC width, α_{BLC}, is calculated from Equation 3. The BLC flux is then calculated by integrating the sine curve from 0° to the α_{BLC}.

The four channels of > 30, > 100, > 300 and > 700 keV are used to create differential energy electron flux spectra. Rather than assuming one specific spectral shape, a combined spectrum is assumed analogous to the proton spectra. The resulting hemispheric electron flux spectra are used to create daily hemispheric electron flux maps. Instead of zonally averaging on L-shell or magnetic latitude, the MP15 routine utilizes Delaunay triangulation to create robust hemispheric maps of electron fluxes. The resulting maps are put into WACCM where the ionization rates are calculated using the Fang et al. (2010) parametrization. Hence, in contrast to the other ionization rates which are computed offline applying a separate background atmosphere, the MP15 ionization rates are computed self-consistently within the WACCM model. The ionization rates are averaged over all MLTs, gridded to a 1.9° latitude and 2.5° longitude, consistent with the WACCM4 grid.

2.8 BCSS-LC

The BCSS-LC estimate provides fluxes and ionization rates for energies of 40-750 keV with a 3-hour resolution.

Low-energy proton contamination is accounted for by utilizing the same corrections as the FRES routine, taking into account the degradation of the proton detectors. Similar to FRES and MP15, cross-contamination of electrons $\gtrsim 750\ keV$ in the proton channel P6 provides an extra electron energy channel (Nesse Tyssøy et al., 2016). Finally, the optimized energy limits and associated geometric factors result in the following four integral channels > 43, > 114, > 292, and > 756 keV(Ødegaard et al., 2017).

The BCSS-LC routine utilizes fluxes from both the $0^\circ$and 90° telescopes to create an estimate of the precipitating fluxes (similar to the Oulu and MP15 estimates). Taking into account the detector response for different pitch angle distributions, the 0° and 90° fluxes are fitted onto the solution of the Fokker-Planck equation for particles (Kennel & Petschek, 1966). A library of equilibrium pitch angle distributions at the equator is calculated and transformed to the satellite altitudes. The orientation of the MEPED telescopes are taken into account, where both the observed and theoretically calculated ratio between the 0° and 90° fluxes are compared. The pitch angle distribution giving the ratio closest to the observed ratio is selected, after which the equivalent isotropic flux level over the BLC is calculated (Nesse Tyssøy et al., 2016). The BLC flux estimate is done separately for each energy channel before the electron flux energy spectrum is estimated by applying the PCHIP interpolation routine. The BCSS-LC model provides the same temporal and spatial resolution as the FRES routine, resulting in geographical maps of 4° latitude and 10° longitude resolution every 3 hours.

Similar to the ApEEP, Oulu and MP15 routines, the ionization rate is calculated by the equation of transfer parametrization by Fang et al. (2010). The background atmosphere is represented by the NRLMSISE-00 model (Picone et al., 2002).

3 Ionization rates intercomparison, March-April 2010

In the following section the different ionization rates are compared for the southern hemisphere during an active geomagnetic period in 2010. April 2010 has previously been shown to cause direct increase of nitric oxide deep into the lower mesosphere in the southern hemisphere (Smith-Johnsen et al., 2017, 2018). Six operating spacecraft including the MEPED telescopes offer a good local time coverage of the MEE precipitation as illustrated in Figure 1. Furthermore, three operating spacecraft observing nitric oxide in the mesosphere enable validation of the ionization rates by comparison with observations of nitric oxide in the mesosphere as presented in the companion paper Sinnhuber et al. (2021).

April 2010 marked the end of the deep solar minimum of solar cycle 24. The upper panel in Figure 3 shows the hourly solar wind speed (black line), V, and the associated northward component of the interplanetary magnetic field (magenta line), B_z. The shaded regions identify the dominant solar wind structures according to Richardson and Cane (2012). Blue shading corresponds to periods of Corotating Interaction Regions (CIRs) or High Speed Streams (HSS), red shading identifies the presence of Coronal Mass Ejections (CMEs). Further, interplanetary shocks are classified according to the Heliospheric Shock Database, generated and maintained at the University of Helsinki (Kilpua et al., 2015). The solar wind gradually increases from Day Of Year (DOY) 91 (April 1), followed by an abrupt increase on DOY 95 (April 5) associated with a fast forward shock marking the start of a CME. The B_z component turns negative late on DOY 95 (April 5) indicating an efficient energy transfer into the magnetosphere confirmed by the geomagnetic indices Disturbance storm time (Dst), Ap, and Auroral Electrojet (AE) in the middle and lower panels in Figure 3. The Ap index maximizes on DOY 95 (April 5), while the Dst index reaches its minima (-81 nT) on DOY 96 (April 6). Based on the AE index weak geomagnetic activity is already ongoing on DOY 91 (April 1) consistent with elevated solar wind speeds. The AE index shows two distinct maxima, a short intense increase on DOY 95 (April 5) reaching approximately 1400 nT, and a more prolonged intensification maximizing at ∼1350 nT on DOY 96 (April 6). The number of substorm onsets identified by Newell and Gjerloev (2011) closely follows the AE evolution with a high rate of substorm onsets during the entire main phase, throughout DOY 96 (April 6). The aftermath of the geomagnetic disturbance is influenced by a CIR structure before it is interrupted by the arrival of a second CME on DOY 101 (April 11). The second CME is, however, embedded in a much weaker solar wind stream, and its associated geomagnetic impact is less intense and of shorter duration. With a Dst below -50 nT, both events can be classified as moderate geomagnetic storms according to Loewe and Prölss (1997). The Dst also indicates some weak geomagnetic storms, $< -30\ nT$ throughout our period of interest.

MEE ionization rates	**AIMOS**	**AISstorm**	**ApEEP**	**ISSI-19**	**FRES**	**Oulu**	**MP15**	**BCSS-LC**
Low energy proton correction	*no*	*no*	*yes*	*yes*	*yes*	*yes*	*yes*	*yes*
Energy channels (keV)	>30 >100 >300	>30 >100 >300	>30 >100 >300	>30 >100 >300	>43 >114 >292 >756	>30 >100 >300	>30 >100 >300 >700	>43 >114 >292 >756
Upper energy limit	300 *keV*	300 *keV*	1000 *keV*	1000 *keV*	756 *keV*	1000 *keV*	1000 *keV*	756 *keV*
Telescopes	0°	0°	0°	0°	0°	0°&90°	0°&90°	0°&90°
Energy spectra	power law	power law	power law	power law	Maxwellian /exponential +power law	power law	Maxwellian/ exponential/ power law	PCHIP
Ionization rate calculation	Monte-Carlo* Wissing and Kallenrode (2009)		Equation of Transfer Fang et al. (2010)		Continuous loss Rees (1989)	Equation of Transfer Fang et al. (2010)		
Background atmosphere	HAMMONIA	HAMMONIA	MSIS	WACCM	CIRA	MSIS	WACCM	MSIS
MLT resolution	6H	0.25–1H	24H	24H	0.7H	24H	24H	0.7H

Table 2: Data handling summary of MEPED electron fluxes used as input for eight different ionization rate estimates. (* includes ionization due to bremsstrahlung.)

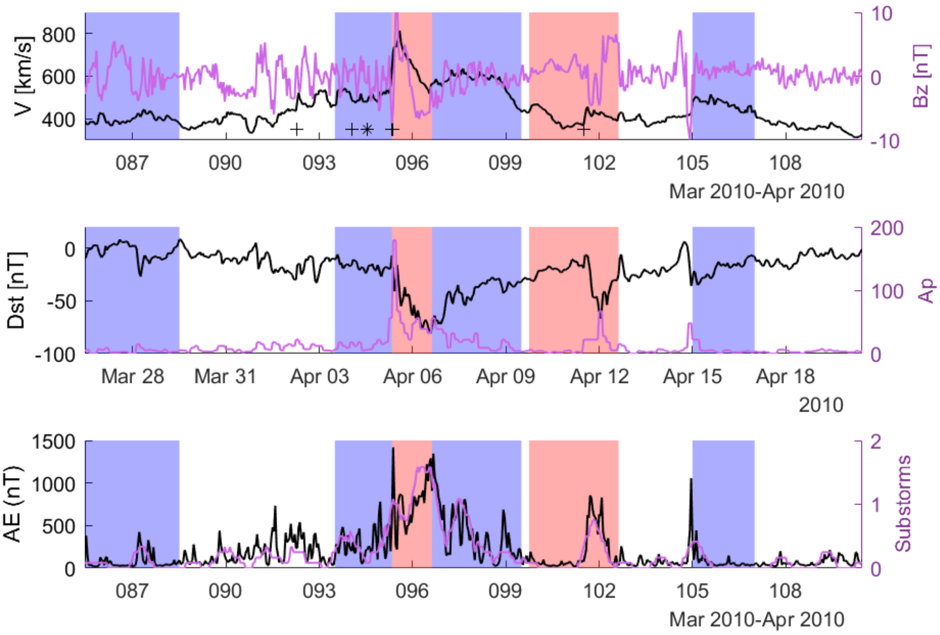

Figure 3: Solar wind parameters and geomagnetic activity indices from March 26 to April 10 2010. Upper panel: Hourly solar wind speed (black), V, and the associated northward component of the interplanetary magnetic field (magneta), B_z. The + and $*$ mark the fast forward and fast reverse interplanetary shocks (Kilpua et al., 2015). Middle panel: Hourly Dst (black) and Ap index (magneta). Lower panel: Hourly AE index (black) and number of substorm onsets per hour (magneta) as a 12-hours moving average (Newell & Gjerloev, 2011). The shaded regions identify the dominant solar wind structure according to Richardson and Cane (2012). Blue shading correspond to periods of CIRs or HSS, red identifies the presence of CMEs.

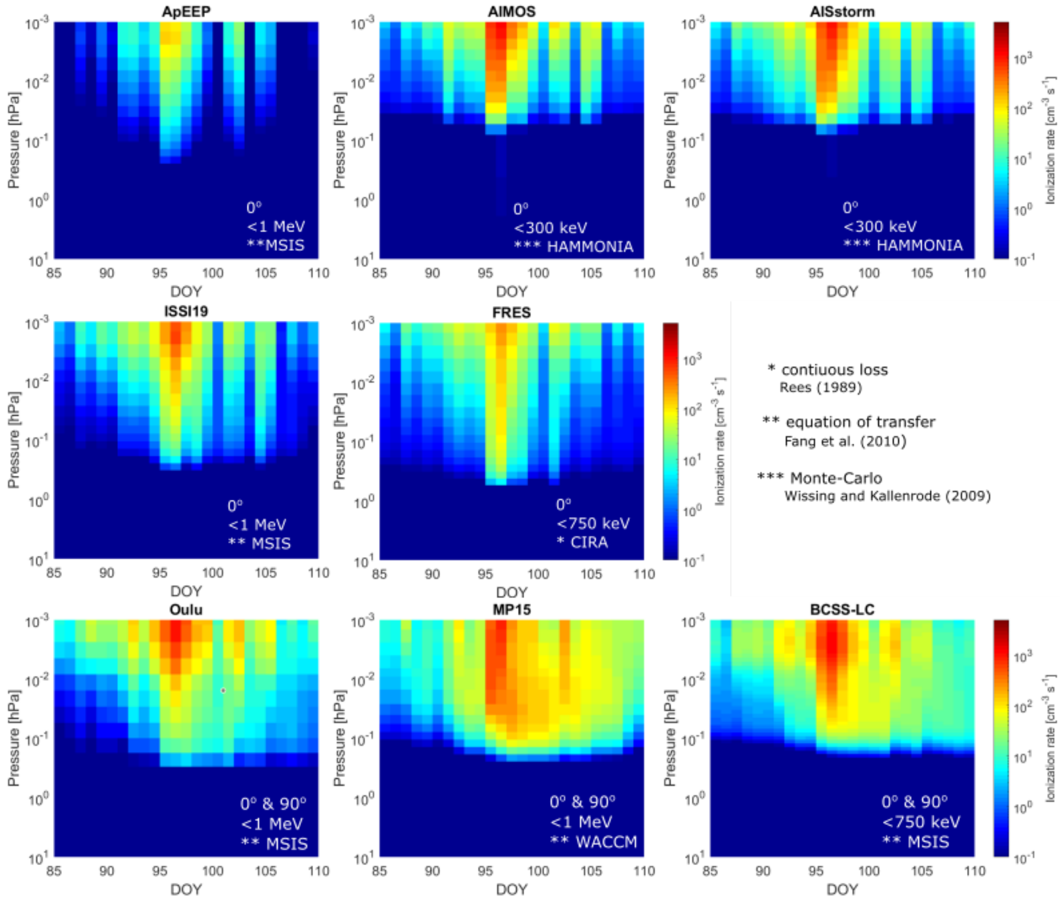

Figure 4: Latitude corrected hemispheric mean poleward of 45°S for the eight ionization rate estimates. The legends list the detector(s), upper energy limit, background atmosphere and ionization rate method applied.

3.1 Hemispheric mean

Figure 4 shows the area-weighted daily hemispheric means of the eight ionization rates averaged poleward of the geographic latitude 45°S. The geographic area cover the main MEE region. A geographic coordinate system is chosen as the subsequent impact on the atmosphere will be governed by atmospheric dynamics and chemistry. The choice of detector(s), upper energy limit, background atmosphere, and ionization rate method applied are listed on each of the subplots. The ionization rates are plotted on a logarithmic scale.

Focusing on the pressure levels that are covered by all ionization rates ($< 5\times10^{-2}$ hPa), the distributions in Figure 4 confirm that the ionization rates based on both the 0° and 90° fluxes (lower panel) are overall larger than the ionization rates based on solely the 0° fluxes (upper and middle panels). These larger values are expected as the 0° detector only measures a small part of the BLC, while the 90° detector typically includes flux contributions from trapped, drift loss cone, and/or contributions BLC, and hence will incorporate substantially larger flux values into the processing. Therefore in the case of an anisotropic pitch angle distribution with decreasing fluxes towards the center of the loss cone, the ionization rates based on the 0° (90°) detector will likely underestimate (overestimate) the EEP flux. The exact level of precipitating MEE fluxes is, however, not possible to validate based on the current available instrumentation. During the main phase of the storm, however, AIMOS, AISSTORM and ISSI19 reach similar levels as the Oulu, MP15 and BCSS-LC rates. This is consistent with a strong substorm onset frequency increasing the wave-particle interaction, leading to strong pitch angle diffusion rates and a more isotropic pitch angle distribution (as reported by Rodger et al. (2013), who contrasted POES satellite observations with ground based precipitation monitoring).

The ApEEP and the FRES ionization rates are notably weaker than the other rates at pressure levels $< 5 \times 10^{-2}$ hPa. Deeper into the atmosphere, $> 5 \times 10^{-2}$ hPa, the FRES ionization rates are comparable or stronger than the ISSI-19 ionization rates. The FRES ionization rates reach, however, unexpectedly high pressure levels compared to the e.g. BCSS-LC ionization rates which cover the same energy range. FRES is the only routine applying the CIRA background atmosphere and the continuous loss method. The FRES ionization rates have been used by Smith-Johnsen et al. (2017) where they found significant correlation between the ionization rates and the NO observations from the Solar Occultation for Ice Experiment instrument on board the Aeronomy of Ice in the Mesosphere satellite down to 55 km.

The output of the ApEEP model provides the lowest ionization rates throughout the period of interest at pressure levels $< 5 \times 10^{-2}$ hPa. At $> 5 \times 10^{-2}$ hPa ApEEP is, however, stronger than AIMOS and AISSTORM as the energy range of the latter two is cut off at 300 keV (see Figure 2). AIMOS and AISstorm is the only ionization rates that include the ionization due to bremsstrahlung. However, the bremsstrahlung effect is orders of magnitudes weaker than the direct ionization by > 300 keV electrons. The apparently low ionization rates from ApEEP, when compared to those from calculations based directly on electron flux observations, have been discussed before by Nesse Tyssøy et al. (2019); Pettit et al. (2019); Mironova et al. (2019). It should, however, be noted that ApEEP is a parameterized model driven by the *Ap* index, designed to capture the solar-cycle variability of the MEE ionization over a 150-year time period. Thus it is not expected to be able to reproduce the ionization rate for individual storms. In this case, for example, the CME embedded in a HSS/CIR structure might not be representative for a typical event of *Ap* around 20 nT. Also, Asikainen and Ruopsa (2016) reported that the strength of the background solar wind speed will influence the strength of the EEP fluxes (> 30 keV), which is not taken into account in the ApEEP model. Recently, Clilverd et al. (2020) validated the ApEEP model during a large geomagnetic storm in March 2015. They found that the ApEEP > 30 keV electron precipitation fluxes were a factor of 1.3

less than the experimentally inferred fluxes during the storm, and were of similar magnitude to the equivalent POES 0° fluxes in the same measurement region.

The MP15 provides the overall strongest ionization rate during the main phase. This is particularly true for the pressure levels $> 5\times10^{-2}$ hPa during the aftermath of the storm. This may be partly attributed to the assumed sine pitch angle distribution with n=1 in Equation 2, which could overestimate the level of isotropy in the pitch angle distribution estimate, and hence the precipitating fluxes. Both the MP15 and BCSS-LC ionization rates suggest a deep ionization maximum around 5×10^{-2} hPa approximately 6 days after the arrival of the first CME structure on DOY 101 (April 6). This feature might be attributed to electrons ($\gtrsim 750\ keV$) observed by the proton telescopes, as MP15 and BCSS-LC are the only methods utilizing the P6 channel as described in Section 2. This is consistent with previously observed time-delayed increases in electrons detected by the MEPED P6 channel (Rodger et al., 2010b). Furthermore, all the ionization rates based on the 0° and 90° detector imply a higher ionization rate level in the aftermath of the storms, while the ionization rates based on the 0° detector alone recover to pre-storm levels within a few days. This is particularly noticeable deeper into the atmosphere. Ødegaard et al. (2017) performed superposed epoch analysis 41 CIR event using the MEPED 0° detector, 90° detector and the derived BLC fluxes. The 0° dectector fluxes fell off faster than the BLC and 90° fluxes. Similarly, Meredith et al. (2011) focusing on CIRs/HSS events reported that the E3 channel peaked 2-4 days later than the storm onset. An evaluation of which data set best predicts the timing of the true MEE precipitation will, however, require observation studies of the MEE precipitation independent of the MEPED instrument.

3.2 Time and altitude evolution

As noted in Section 1, the observed downward transport of NO during winter is an active research topic along with the climate models' capability of reproducing it (Smith-Johnsen et al., 2018; Pettit et al., 2019). Therefore, accurate knowledge of the time and altitude evolution of the ionization rates is essential to interpret the subsequent impact on, e.g., NO abundances in the atmosphere. Figure 5 shows the area-weighted hemispheric mean (> 45° S) ionization rates at pressure levels 0.01 hPa (∼ 80 km) and 0.1 hPa (∼ 64 km). The ionization rates are plotted on a linear scale. Consistent with the gradual increase of solar wind speed from DOY 91 (April 1), a weak intensification in several of the ionization rates is observed at the upper altitude 0.01 hPa (∼ 80 km) and a few days later at the lower altitude 0.01 hPa (∼ 64 km). The fast forward solar wind shock on DOY 95 (April 5) marks the start of the CME impact on the magnetosphere. The precipitating electron fluxes intensify at all energy levels, resulting in an estimated ionization rate increase deep into the lower mesosphere.

Driven by the time-varying Ap index, the ApEEP ionization rate maximizes at April 5 (DOY 95) and decreases only slightly through April 6 (DOY 96). At the higher altitude, the same is the case for MP15 rate, while the AIMOS and AISstorm rates predicts similar intensity levels on DOY 95 and 96. While showing an intensification on DOY 95, all other ionization rates maximize on DOY 96 at pressure level 0.01 hPa (∼ 80 km). This one day offset is also evident in the Ap index and the Dst index, as shown in Figure 3.

All ionization rate estimates also agree on an intensification in ionization rates on DOY 101-102 (April 11-12) and DOY 104-105 (April 14-15). The ionization rates on DOY 101-102 are associated with a second CME structure, while those on DOY 104-105 are linked to a CIR structure. However, there is a prominent difference between the rates based on data from only the 0° detector compared to those rates based on both the 0° and 90° detectors during these secondary intensifications. The ionization rates based on the 0° detector are comparable to the weak pre-storm increase around DOY 91-94. How-

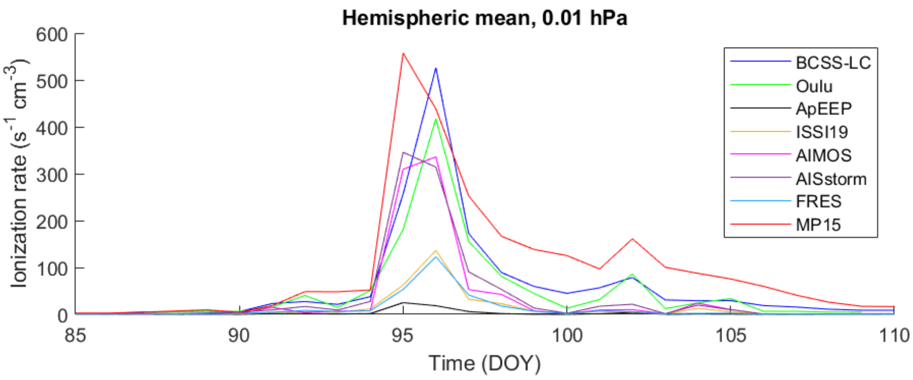

(a)

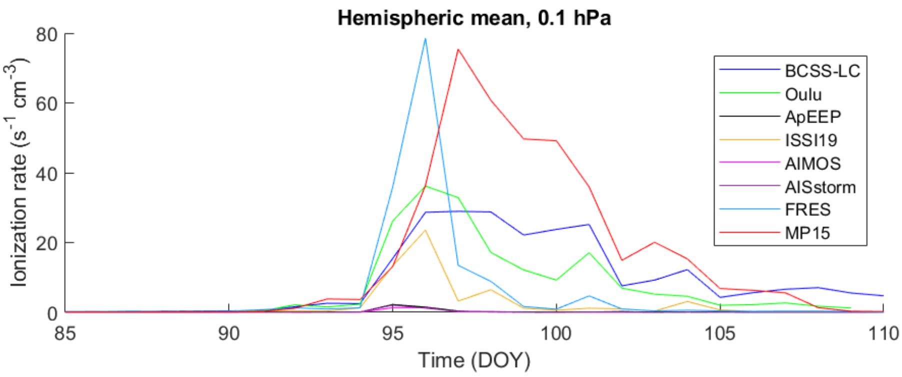

(b)

Figure 5: Latitude corrected hemispheric mean poleward of 45°S for the eight ionization rate estimates produced by the different processing techniques, shown at two distinct pressure surfaces 0.01 hPa ($\sim$ 80 km) (upper panel) and 0.1 hPa ($\sim$ 64 km) (lower panel). Note that 0.1 hPa is outside of the nominal pressure range of AIMOS and AISstorm as shown in Figure 2.

ever, the ionization rates based on the 0° and 90° detectors, OULU, MP15 and BCSS, are generally higher compared to the pre-storm level. In fact, for the MP15 ionization rates the secondary storm period rate constitutes 1/4 of the total ionization at 0.01 hPa (80 km) from DOY 96-105. In contrast, for the AISstorm rates, only 1/10 of the total ionization at 0.01 hPa (80 km) occurs during the secondary storm period. The ionization rate differences during this period are possibly due to an increased population of radiation belt electrons associated with the main event, where only weak substorm activity is necessary to push the weakly trapped electrons into the loss cone, along with increased trapped fluxes present in the 90° detector data. The subsequent anisotropic pitch angle distribution will likely cause an underestimate of the loss cone fluxes for techniques which are based only on observations by the 0° detector near the center of the loss cone, while the techniques incorporating both detectors will compensate for this but rely on assumptions concerning the pitch angle distribution of the fluxes. Temporal variations between the ionization rates can also be a consequence of the choice of satellite observations. The EPP region shows MLT flux differences of about a factor 30, which also relocate during substorm periods. This implies that satellites covering different MLT regions may record different fluxes. Therefore, the model specific up-scaling of sparse satellite measurements onto global coverage may affect the results. OULU is based on measurements from dawn and dusk only, while MP-15, BCSS-LC, FRES, ISSI-19 applies all satellites available. These will be more sensitive to short time changes in comparison to ApEEP giving an average representation. AIMOS as well as AISstorm handle up-scaling by a comparison with long-term averages which has down-sides on specific events, but allows a rather easy handling of MLT (or orbit) variations.

At 0.1 hPa ($\sim\ 64km$) the ApEEP, AIMOS, and AISstorm models have only minor contributions as pointed out above. The FRES routine suggests the highest maximum ionization rate for this pressure level on DOY 96. In comparison to the loss cone estimates this seems exaggerated possibly due to the simplistic background atmosphere and/or inaccurate based on the goodness of fit in respect to the assumed spectral shape. Based on the FRES-WACCM comparison with SOFIE in Smith-Johnsen et al. (2018), the FRES ionization rates appear to overestimate the direct impact associated with the first CME. The timing of the maximum ionization rates agrees, however, with the Oulu and ISSI-19 ionization rates. The FRES and ISSI-19 ionization rates drop off quickly with time during this period, showing only a weak impact of the secondary storms. The BCSS-LC ionization rate data-set shows, however, elevated, fairly constant ionization rate throughout several days from the main event and the second CME event. The OULU data-set estimates similar values to the BCSS-LC but has a clearer distinction between the two CME-storms. The MP-15 produces the largest total ionization rate impact.

Several atmospheric model studies have found an underestimate in the lower mesospheric and upper stratospheric NO density. The topical debate has been to which extent this is related to ionization rate deficiencies and/or downwelling rate throughout the mesosphere and lower thermosphere during winter (Randall et al., 2007; Hendrickx et al., 2018; Pettit et al., 2019). It is evident that the timing and intensity of the mesospheric ionization rates fuels the discussion to which degree it could be partly driven by an underestimation of the direct ionization. Furthermore, the MEE ionization rate profile itself is important also for the indirect effect, as the production at any altitude level will add to the indirect effect at the levels below (Smith-Johnsen et al., 2017, 2018).

3.3 Spatial EEP region

The indirect effect of downward transported EPP-produced NO will depend on the geographic latitude distribution of the ionization rates, as the strength of the downwelling is expected to be stronger inside the polar vortex area compared to mid-latitudes. Further, EPP-produced NO at mid latitudes might be more exposed to photolysis during wintertime compared to EPP-produced NO at high latitudes. Figures 6 - 8 show the ion-

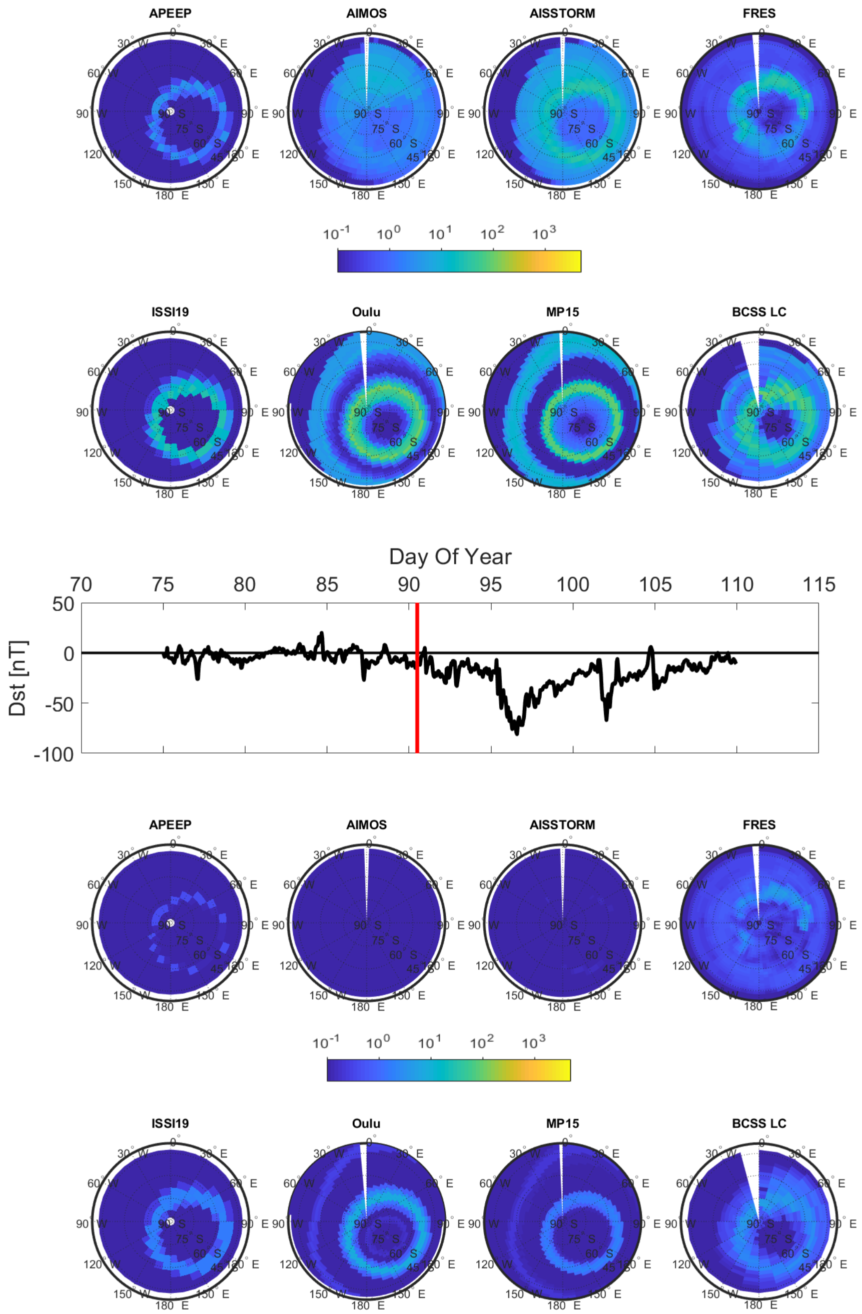

Figure 6: Maps of the ionization rate in the Southern hemisphere at two distinct pressure levels: 0.01 hPa (∼ 80 km) (upper panels) and 0.1 hPa (∼ 64 km) (lower panels) for DOY 90 (March 30) 2010 (before the onset of the geomagnetic storm). Note that 0.1 hPa is outside of the nominal pressure range of AIMOS and AISstorm as shown in Figure 2. The time changing level of geomagnetic activity is shown in the Dst index (middle panel.)

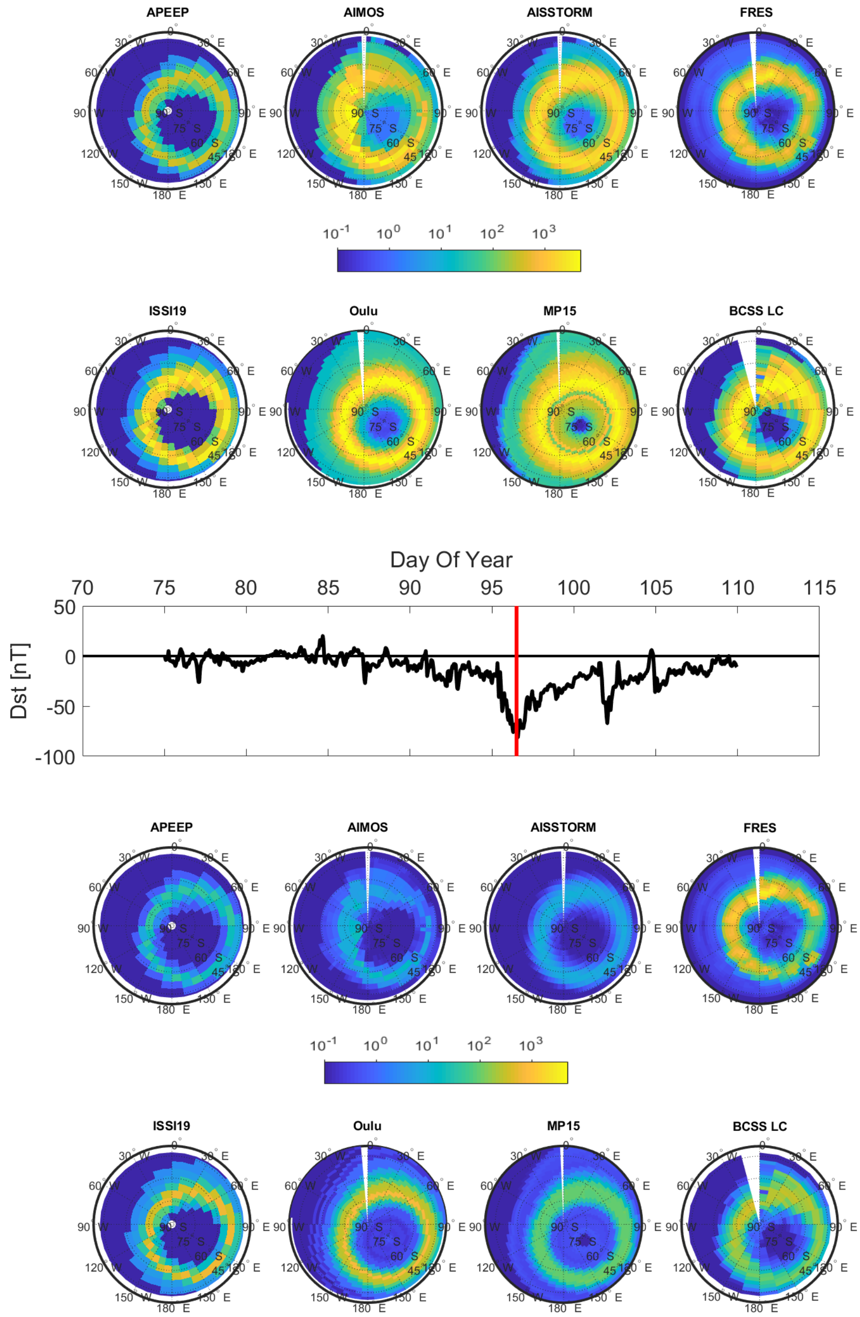

Figure 7: Same as Figure 6 for DOY 96 (April 6) 2010 (during the storm).

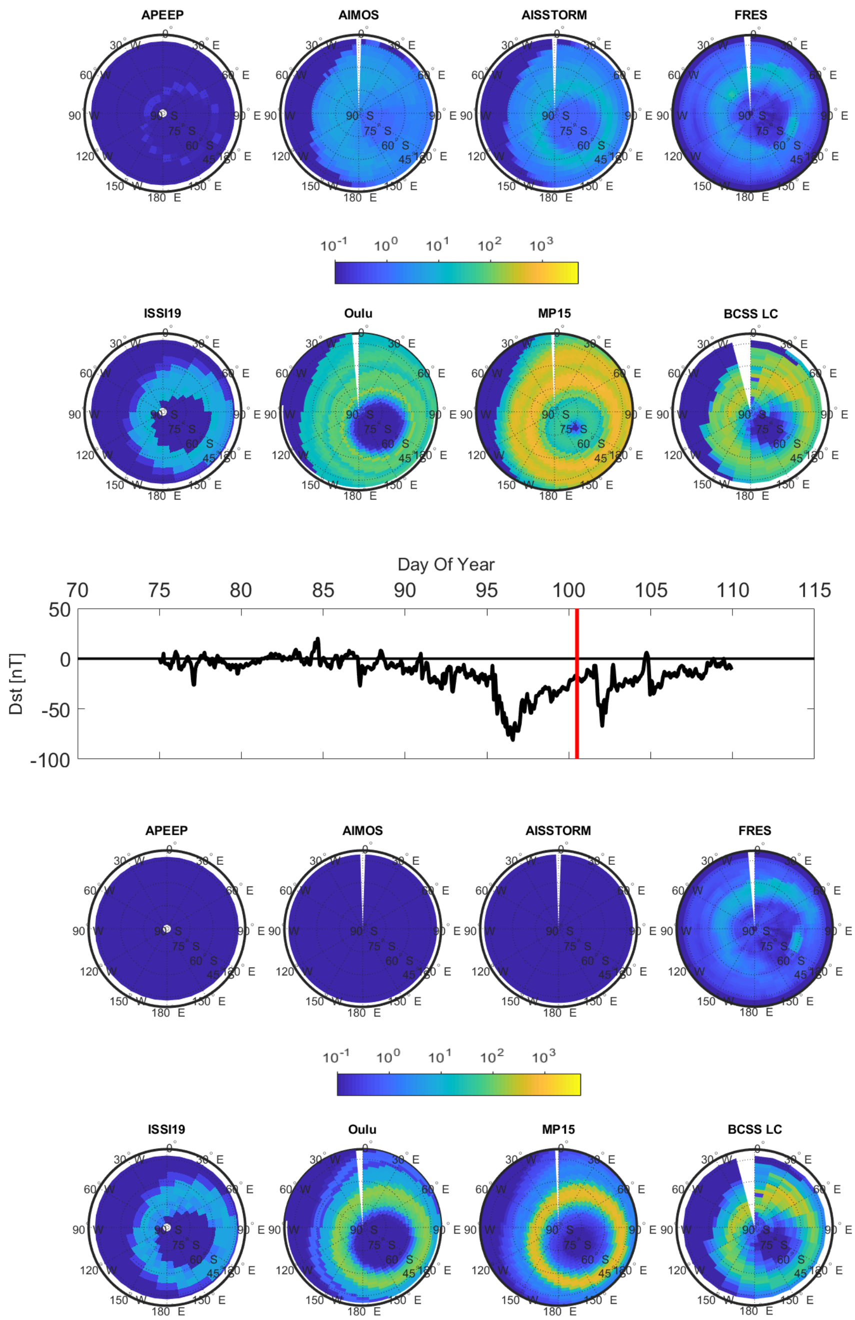

Figure 8: Same as Figure 6 for DOY 100 (after the first storm period).

ization rates at 0.01 hPa ($\sim$ 80 km) and 0.1 hPa ($\sim$ 64 km) in the pre-storm (DOY 90, Figure 6), main storm (DOY 96, Figure 7) and recovery phase (DOY 100, Figure 8), respectively. In each of these three figures the eight upper plots show the ionization rate distribution at pressure level 0.01 hPa ($\sim$ 80 km) and the eight lower plots show the ionization rate distribution at pressure level 0.1 hPa ($\sim$ 64 km) for the SH.

As shown in Figure 6, DOY 90 (March 30) is characterized by quiet geomagnetic activity and low levels of ionization at both pressure levels. Due to the nature of the respective ionization rate data-sets, ApEEP, ISSI-19, Oulu, and MP15 are zonally averaged in geomagnetic coordinates, while AIMOS, AISstorm, FRES, and BCSS-LC vary with MLT/in longitude. Nevertheless, for 0.01 hPa ($\sim$80 km) the largest discrepancy is related to the total extent of the auroral oval. ApEEP shows the lowest ionization rate as well as the most confined MEE region. Both ApEEP and ISSI-19 have a wide polar cap with zero ionization, while e.g. AIMOS, AISstorm and MP15 have weak, but non-zero ionization over the polar cap. The ionization rates based on observations from both the 0° and 90° detectors, MP15, OULU and BCSS-LC, estimate the highest quiet-time ionization rates and the widest precipitation region. In particular, MP15 and OULU show a characteristic double oval feature. The two regions of precipitation are separated by a distinct minimum extending over several degree of latitude. (Note, that this is can not be attributed to different treatment of the SAA as all routines exclude this area.) The double oval feature is less prominent at 0.1 hPa ($\sim$ 64 km). At 0.1 hPa ($\sim$ 64 km) Oulu shows the strongest ionization followed by BCSS-LC and MP15. AIMOS and AISstorm data-sets estimate the weakest ionization rates due to its upper energy limit at 300 keV implying that only ionization due to bremsstrahlung will contribute at this pressure level.

At DOY 96 (April 6, Figure 7), where the Dst reaches the minimum value in the main storm, both the ionization rate and geographical coverage are enhanced for all the ionization rates. Similar to the quiet periods, at 0.01 hPa ($\sim$ 80 km) the MP15 data-set produces the most intense ionization rates with the most extensive coverage, both poleward and equatorward. The ApEEP data-set shows the lowest ionization rate. For both ApEEP and ISSI-19 the oval widens equatorward while the poleward boundary remains constant. In contrast to those data-sets, MP15 has elevated ionization rates also in the polar cap separated by a minimum from the main EEP region. For the MP15 and the Oulu ionization rates, the distinct minimum shown in Figure 6 is no longer evident. At 0.1 hPa ($\sim$ 64 km) the FRES routine estimates the most intense oval, followed by Oulu and ISSI-19. Both AIMOS and AISstorm predict elevated ionization rates due to bremstrahlung, but it remains approximately an order of magnitude less than the comparatively modest ApEEP prediction. The polar cap is now wider for all ionization rate data-sets and there is good agreement in regard to the size of the EEP region between the different approaches.

In the recovery phase of the main storm on DOY 100 (April 10, Figure 8) there are large discrepancies in both the intensity and the size of the precipitation region at both pressure levels. The largest difference is found between the routines based on both the 0° and 90° detector compared to the routines based on only the 0° detector. The ApEEP ionization rates estimate the weakest and most confined EEP region. The MP15 data-set predicts the strongest and widest EEP region. The apparent polar cap filling of this data-set could be a side effect of the mapping function. MEEs originate from the radiation belts and possibly the plasmasheet, and are not expected to fill the polar cap. But it is likely that when used as input in a climate model, a larger fraction of the total ionization will be available to be transported vertically downwards compared to e.g. the OULU routine or ISSI-19 which have fairly wide polar caps with no ionization. The downwelling will depend on the specific dynamical conditions. The period April 2010 is early fall in the SH and the downward transport is weaker compared to winter. At 0.1 hPa ($\sim$ 64 km) significant ionization rates are predicted by all routines except ApEEP, AIMOS and AISstorm. The estimates, however, vary by more than an order of magnitude between the two-detector estimates of OULU, MP15, and BCSS-LC, and the estimates based solely on the 0° detector FRES and ISSI-19.

3.3.1 A double EEP region

Both the OULU and MP15 ionization rates depict precipitation regions with multiple maxima and minima as function of latitude. The BCSS-LC ionization rate also shows some tendencies of some lower latitude intensification in some regions, which if zonally averaged might bear similarities to the OULU and MP 15 routines. The ionization rates based on the 0° detector only show single maximum EEP regions peaking at a given magnetic latitude. This raises the question whether the lower latitude EEP regions represent real energetic electron precipitation, or if it is overestimated by the methods applying both the 0° and 90° detector.

EEP is driven by wave-particle processes such as VLF whistler mode chorus waves, plasmaspheric hiss waves, and electromagnetic ion-cyclotron (EMIC) waves (Summers et al., 2007). The plasmapause represents the outer boundary of the plasmasphere which is populated by dense and cold plasma. As the electromagnetic waves strongly depend on the medium it propagates in, the plasmapause marks an abrupt change in the characteristics of the wave-particle interaction. Chorus waves are expected to largely control electron precipitation processes outside of the plasmasphere (Whittaker et al., 2014). EMIC-driven precipitation processes tend to occur close to the outer edge of the plasmasphere (Carson et al., 2013), while plasmaspheric hiss can cause weak EEP fluxes within the plasmasphere (Hardman et al., 2015), as do lightning-generated whistlers (Voss et al., 1998; Rodger et al., 2007). The secondary oval features appear at geomagnetic midlatitudes, which imply that, if real, the EEP should follow the nature of plasmaspheric hiss.

Plasmaspheric hiss can persist during relatively quiet conditions, and largely account for the formation of the slot region that separates the inner and outer radiation belts. During storms or substorms the emission intensifies associated with the injection of plasma sheet electrons into the inner magnetosphere. The minimum resonant energy increases with decreasing L, whereby hiss will contribute to EEP up to 1 MeV. The global distribution of hiss indicates a strong day-night asymmetry favoring the dayside. This is, however, influenced by the level of geomagnetic activity (Hardman et al., 2015).

The double maxima are unified in the main phase of the storm. This is consistent with Kavanagh et al. (2018) who identify DOY 94 (April 4) as a slot region filling event. This implies that the slot region between the outer and inner radiation belt are populated with energetic electrons. Afterwards, the slot region will again be carved out by resonant wave-particle interactions with plasmaspheric hiss, and Figure 8 shows that the double feature emerges again around DOY 100 (April 10) in both Oulu and MP15 ionization rates. Further, the radiation belt decay rates due to plasmapheric hiss are on the order of a few days for $\sim$500 keV electrons (Ni et al., 2013). This relative weak pitch angle scattering rate suggests a strong anisotropic pitch angle distribution within the loss cone which might explain why the secondary EEP region is not evident in the ionization rates based on the 0° detector.

On the other hand, there is a distinct possibility that the loss cone estimates are exaggerating the ionization rate intensity considering the applied methods. In the MP15 and BCSS-LC datasets the determination of the BLC fluxes rely on measurements from both 0° and 90° detectors in order to determine the shape of the pitch angle distribution. Hence, the level of the uncertainty of the BLC fluxes grows when the 0° fluxes are close to the noise floor and their true value is hard to determine(Nesse Tyssøy et al., 2016, 2019). The OULU routine, which uses the mean of the log fluxes of the 0° and 90° detectors, without accounting for the change in the telescope viewing geometry as function of latitude like the MP15 and BCSS-LC routine, may incorporate trapped or DLC

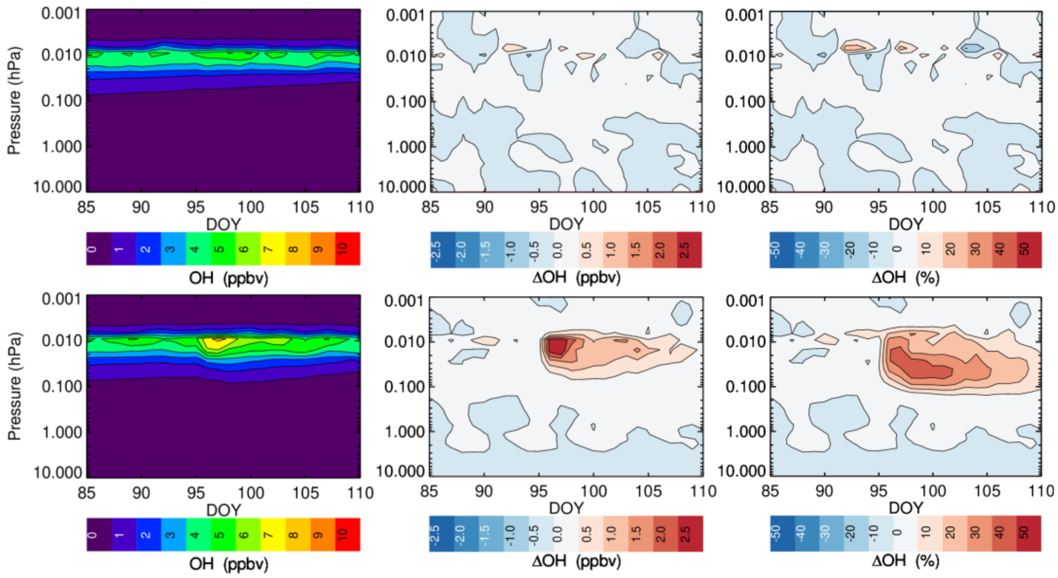

Figure 9: Left row: The OH daily hemispheric mean (ppbv) poleward of 45°S estimated by WACCM6 based on the MEE ionization rates ApEEP (upper panel) and MP15 (lower panel). Middle (right) row: The absolute (percentage) difference in OH density in respect to a baseline simulation without MEE ionization rates.

inner radiation belt electrons sampled by the 90° detector into the BLC flux resulting in an overestimate. Hence, the existence and level of ionization of a possible secondary EEP region needs to be validated by other means which are out of the scope of the present study.

4 The response of an atmospheric model to extremes of MEE forcing

The ionization due to EEP into the atmosphere initiates a series of chemical reactions increasing the production of HO_x and NO_x species, both of which contribute to ozone loss in the stratosphere and mesosphere. In the following, we assess the range of chemical OH and NO impact caused by MEE, as simulated with the WACCM model. To do this, we implement the data-sets which provide the lowest and highest ionization rates, i.e. ApEEP and MP15. The objective is to evaluate the uncertainty regard the estimated MEE impact on the atmosphere.

WACCM is an atmopheric component of the Coupled Earth System Model, *CESM* (Hurrell et al., 2013). In the current study we have applied WACCM version 6 in the specified dynamics mode. It has a vertical extent from the Earth's surface to 6×10^{-6} hPa ($\sim$ 140 km) divided into 88 pressure level layers. Horizontal resolution is $0.95°\times1.25°$ in latitude×longitude. For the specified dynamics mode, temperatures and winds below $\sim$50 km are nugded to the NASA Global Modeling and Assimilation Office's Modern-Era Retrospective Analysis for Research and Applications (MERRA) version 2. More details can be found in Gettelman et al. (2019). Here, model version 6 is applied. It includes a detailed ion chemistry scheme which extends the model ionosphere to mesospheric and stratospheric altitudes and allows for the response to ionization due to MEE, solar protons, and galactic cosmic rays to be simulated without simplifying parameterizations (Verronen et al., 2016). This representation of the lower ionosphere is based on the analysis of the 1-D Sodankylä Ion and Neutral Chemistry model (Verronen & Lehmann, 2013), and provides improved response to EPP and a better agreement with satellite-based observations (Andersson et al., 2016). The auroral EEP is identical for the two model runs scaled by the Kp index, which enables us to target the different chemical responses to the different MEE ionization rates. We perform three model simulations with different MEE forcing: 1) without MEE (baseline), 2) the ApEEP ionization rates, and 3) the MP15 ionization rates.

Figure 9 shows the estimated OH level in parts-per-billion-volume (ppbv) as a area-weighted hemispheric average poleward of 45°S for the ApEEP (upper panel) and MP15 (lower panel) ionization rates. The background level is dominated by UV photolysis of water vapour and MEE drizzle. Attributed to positive ion-chemistry involving water cluster ions, increased ionization will transfer H_2O into HO_x (Verronen & Lehmann, 2013). Above 80 km there is not sufficient water vapor to form water cluster ions, needed in the EEP-HOx production (Solomon et al., 1981; Sinnhuber et al., 2012). Hence, both model runs have a rather sharp upper boundary just above $\sim$ 0.01 hPa ($\sim$ 80 km). The lower boundary, on the other hand, is governed by the UV photolysis and the MEE ionization penetration depth. During the main event, starting on DOY 95, it is evident that the MP15 ionization rate penetrates deeper into the lower mesosphere compared to the ApEEP ionization rate.

The second and third column of Figure 9 show the difference in absolute ppbv as well as percentage difference in respect to the baseline simulation where the MEE is set to zero. As odd hydrogen has a lifetime of a few hours only (Crutzen & Solomon, 1980), the OH variability strongly follows the MEE ionization rates. Although the MP15 has higher background ionization in the quiet period compared to ApEEP, this is barely evident in the OH concentration because the background distribution is dominated by UV photolysis of water vapour. Further, the changes relative to the baseline simulation are barely evident in the ApEEP simulation at any pressure level. The lack of response in ApEEP suggests that there is a threshold limit in the MEE ionization rates for it to be important for OH as confirmed by observations, see, e.g., (Verronen et al., 2011; Häkkilä et al., 2020). For MP15, the difference, however, becomes prominent from DOY 95 till DOY 110. At 0.01 hPa ($\sim$80 km) the MP15 ionization rate creates up to $\sim$ 2.5 more OH ppbv, corresponding to $\sim 20-40\%$ higher density compared to the reference simulation. Although the absolute difference is less near 0.1 hPa ($\sim$64 km), the percentage difference is more prominent at the lower edge of the OH layer. Based on the OH peak in the main phase of the storm, the impact of the lowest and highest ionization rates on OH differs by a factor of $\sim$ 1.5 in the middle and lower mesosphere.

Figure 10 shows the modelled NO level in parts-per-billion-volume (ppbv) as a hemispheric average poleward of 45°S for the ApEEP (upper panel) and MP15 (lower panel) ionization rates estimates. As the auroral forcing is the same in both model runs the difference can be ascribed to the different MEE ionization rates. Applying the MP15 ionization rates, higher levels of NO are evident already in the quiet period (DOY 85 to 95). This implies that the weak MEE drizzle during the pre-storm event raises the NO background level using the MP15 ionization rates compared to the ApEEP ionization rates. Due to the long lifetime of NO, approximately one day under sunlit conditions (Bender et al., 2019), the NO densities will at any point in time be the cumulative sum of the NO impact. This is why the NO densities based on these ionization rates, peaks a few days after the ionization rate peaks at the respected altitudes. In the main phase and recovery period of the first storm (DOY 95-100) NO enhancements are visible down to $\sim$ 0.05 ($\sim$ 70 km) using the ApEEP ionization rates, and down to $\sim$ 0.1 hPa ($\sim$ 64 km) applying the MP15 ionization rates.

The second and third column of Figure 10 show the difference in absolute ppbv as well as percentage difference in respect to a baseline simulation where the MEE is set to zero. At $\sim$ 0.01 hPa ($\sim$80 km), in the main phase of the storm, the NO densities based on the ApEEP ionization rates give an NO density increase $\sim$10-50 ppbv corresponding to $\sim 50-100\%$ compared to the baseline. Based on the MP15 ionization rates the

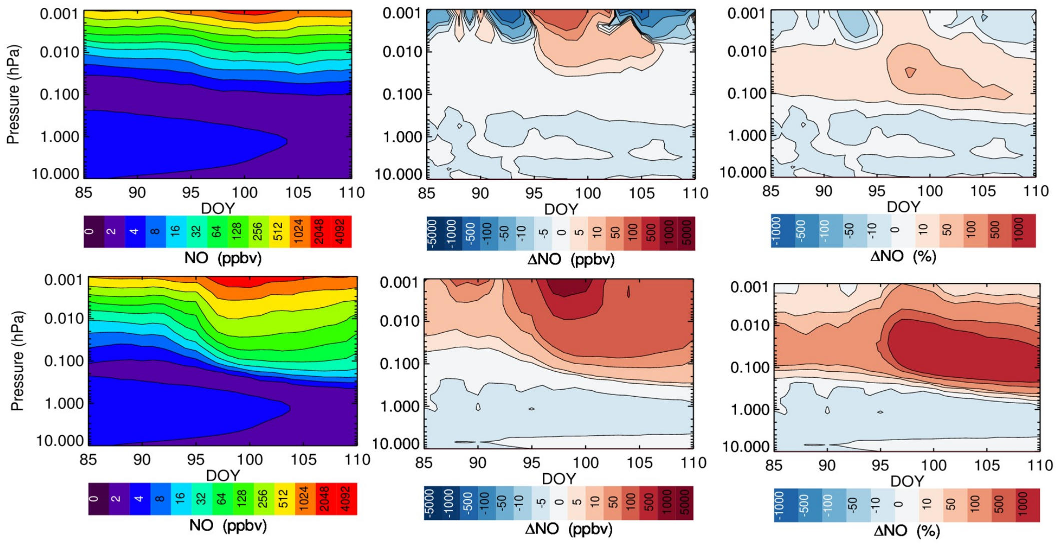

Figure 10: Left row: The NO daily hemispheric mean (ppbv) poleward of 45°S estimated by WACCM6 based on the MEE ionization rates ApEEP (upper panel) and MP15 (lower panel). Middle (right) row: The absolute (percentage) difference in NO density in respect to a baseline simulation without MEE ionization rates.

increase is ~50-100 ppbv, corresponding more than ∼ 1000% compared to the baseline. The MP15 ionization rates produce NO increases that are larger than ∼ 1000% throughout the entire middle and lower mesosphere, while the ApEEP ionization rates result in an increase of ∼ 20% compared to the baseline run. The difference subsists throughout the entire observation period. Further, it is evident that the lower mesospheric NO from both model runs penetrates deeper into the atmosphere during and after the event, consistent with a slow, but steady downward transport.

Based on the current comparison, NO is in the range of 4-32 ppbv for ApEEP and 32-256 ppbv for MP15 in the middle and lower mesosphere during and after the geomagnetic active period. This implies the impact of the lowest and highest ionization rates result in a difference of a factor of ∼ 8. However, the uncertainty related to the MEE impact on NO will be influenced by the strength of the downwelling and the intensity of the photolysis which both determine the cumulative response. April corresponds to the early fall season in the SH. Due to this, the downward transport is weaker compared to winter, and it is not yet polar darkness. Therefore, the uncertainty related to the MEE impact on NO will be influenced by the season, likely higher than shown here during midwinter, but lower during summer.

5 Discussion and Summary

The quantification of MEE impact on the atmosphere has long been an outstanding question. Here we compared eight different ionization rate estimates, all based on the MEPED observations: AIMOS, AISstorm, ApEEP, FRES, ISSI19, OULU, MP15, and BCSS-LC. Different data handling, in form of correction of the electron detector's spurious response to protons, the degradation of the proton detectors, the choice of telescopes, electron energy channels and energy limits, spatial and MLT sampling, as well as shape of energy spectra, all contribute to different flux estimates. Further discrepancies might arise due to different methods of calculating the ionization rates and choice of background atmosphere. The main objective of the intercomparison is to examine the uncertainty related to the MEE ionization rates and the associated impact on the atmosphere. Based on a case study period spanning 25 days during March and April in 2010, we summarize the following findings:

- The different ionization rates agree reasonable well in terms of the temporal variability.
- The ionization rates based on both the 0° and the 90° detector are generally higher than the ionization rates based solely on the 0° detector.
- The most extreme ionization rates differ by orders of magnitude both during geomagnetic quiet and disturbed periods.
- The largest discrepancies are found in the recovery phase of the geomagnetic storm period.

A robust recommendation concluding which of these eight ionization rate estimates provides the most realistic representation of MEE ionization requires an independent validation in the form of direct electron flux observations and/or observations of the atmospheric impact such as electron density, bremsstrahlung, cosmic radio noise absorption, or chemical changes. The latter will be limited by the accuracy of the observations, as well as the models used to estimate the impacted variables from the ionization as demonstrated in the companion paper Sinnhuber et al. (2021). Due to inadequate pitch angle coverage, most of the current particle detectors in space are unsuitable for accurately determining the flux of MEE precipitating into the atmosphere. There is also the question of how to convert the existing measurements, with their limitations, into accurate energy resolved precipitating fluxes. In the future, newly launched and planned cubesat missions might be able to validate the MEPED data handling applied in the ionization rate routines. At the moment, the current study provides an upper and lower bound of the potential MEE ionization rates. Furthermore, it is important to emphasis that any future recommendation will depend on the intended use of the ionization rates in terms of e.g. time coverage, MLT resolution, event studies, and altitude levels:

- Time coverage: ApEEP is the only ionization rate dataset currently available for long term studies providing data from 1850 up to now. Oulu provide global ionization rates from 1979 up to now. All the other ionization rates cover the time period of the SEM2 detector from 1998 and onwards.
- MLT and temporal resolution: All of the ionization rates presented here are given with daily resolution. AIMOS, AISTORM, FRES and BCSS-LC routine provide the ionization rates on 2 hours and 3 hours resolution. AIMOS, AISTORM, FRES and BCSS-LC also offers a longitude/MLT resolution and might therefore be applicable for more localized and shorter events.
- Event specific ionization rates: ApEEP, AIMOS, and AISTORM are scaled and partly scaled by geomagnetic indices, which implies that ISSI-19, FRES, Oulu, MP15, and BCSS will be better suited to represent extraordinary events.
- Lower mesosphere: AIMOS and AISTORM upper energy limit implies that the direct ionization rates stop at ∼70 km, while ApEEP, ISSI-19, Oulu and MP15 will potentially reach ∼60 km. FRES and BCSS-LC are stopped slightly higher than ∼60 km.

Depending on the scientific goals considered, different datasets will be more or less suitable.

Furthermore, we demonstrate that the discrepancies between the ionization rates are not linearly scaled to the differences between the ionization rates. The most extreme ionization rates, with the largest and smallest rates from the set of eight, were produced by MP15 and ApEEP. The rates from those two approaches are used as input in the chemistry climate model WACCM version 6. Evaluating the short term impact on the mesospheric OH and NO density we find:

- Although significantly different ionization rates, the MEE precipitation associated with the pre-storm drizzle has little impact on OH. For the ApEEP ionization rates, even during the main event the precipitation has no significant effect on OH. The storm time impact of the lowest and highest ionization rates on OH differs by a factor up to 1.5 in the middle and lower mesosphere. This discrepancy is maintained throughout the recovery phase of the storm.
- For the NO production, the effect of the different MEE ionization rates are evident also during the pre-storm condition. In the geomagnetic active period, including the recovery periods, the NO concentration differs by a factor of ∼8 in the middle and lower mesosphere. Based on MP15 ionization rates an increase in NO concentration of up to 1000% in respect to the baseline run will reach the lower mesosphere ($\sim 60\ km$) approximately two weeks after the storm onset.

The lack of response to the ApEEP ionization rates indicate that there is a threshold for MEE forcing which must be exceeded to have an observable response in OH, see e.g., Verronen et al. (2011); Häkkilä et al. (2020). This implies that the choice of MEE ionization rate will not largely impact the amount of OH in a model during geomagnetic quiet and minor geomagnetic storms. On the other hand, Zawedde et al. (2016) showed applying the BCSS-LC fluxes in conjunction with OH observations that there is substantial EEP-driven OH production even during minor to moderate geomagnetic events. Furthermore, Zawedde et al. (2018) suggested that the MEE OH-production efficiency may be constrained by the water vapour level at the production altitude which will vary with e.g. season.

In contrast to the chemically short lived OH, the long lifetime of NO during polar winter implies that the differences in atmospheric response between the MEE forcing extremes will strongly depend on season and the dynamical conditions. It is therefore likely that the discrepancy in the modelled NO will increase over the winter season due to less photolysis occurring, stronger confinement of the MEE produced NO at polar latitudes, and stronger residual downward transport. The long term NO levels induced by the upper and lower MEE ionization rates NO projected by the ionization rate extremes will be the subject of a future study. It should, however, be noted, that the ApEEP model, being recommended as part of the Solar Forcing for CMIP6 (v3.2) and therefore frequently used to evaluate the impact of MEE on the atmosphere, represents the lower bound of all eight models compared here, and therefore most likely represents a lower limit estimate of the impact of MEE precipitation into the atmosphere in current climate studies.

In summary, this intercomparison experiment quantifies the uncertainty related to the available MEE ionization rate. It will enable quantitative studies of the importance the atmospheric impact, as well as an evaluation of the relative importance of MEE compared to other ionization sources, such as aurora, SPEs, solar flares (EUV) and galactic cosmic rays using the upper and lower bound. In the companion paper, Sinnhuber et al. (2021), the validity of three of these ionization rate data-sets, ApEEP, AIMOS, and OULU, is evaluated by comparing the output of four chemistry-climate models to observed NO densities. There we find that the differences in the amount of NO in the individual models are much larger than the differences between the multi-model mean using different ionization rates, however, multi-model mean results are consistent with the differences between ionization rate data-sets used. This implies that the MEE ionization rates are only one of several aspects governing the atmospheric NO budget in chemistry-climate models.

Acknowledgments

This paper as well as the companion paper are a collaborative effort of the working group five: Medium Energy Electrons (MEE) Model-Measurement intercomparison of the SPARC Solaris-Heppa initiative, see `solarisheppa.geomar.de`. We thank the SPARC/WCRP for supporting the initial working group meetings.

H. Nesse Tyssøy is supported by the Norwegian Research Council (NRC) under contract 223252 and 302040. S. Bender and C. Smith-Johnsen are also supported by the NRC under contract 223252. T. Asikainen is supported by the Academy of Finland (PROSPECT project no:321440). B. Funke acknowledges financial support from the Agencia Estatal de Investigación of the Ministerio de Ciencia, Innovación y Universidades through projects ESP2017-87143-R and PID2019-110689RB-I00, as well as the Centre of Excellence "Severo Ochoa" award to the Instituto de Astrofísica de Andalucía (SEV-2017-0709). J. Pettit's work is funded by NSF CEDAR grant AGS 1651428. E.Rozanov's and T. Sukhodolov's work on the manuscript is done in the SPbSU "Ozone Layer and Upper Atmosphere Research Laboratory" supported by the Ministry of Science and Higher Education of the Russian Federation under agreement 075-15-2021-583 and was partly supported by German Russian cooperation project "H-EPIC" funded by the Russian Foundation for Basic Research (RFBR project No 20-55-12020). M. Sinnhuber work was partly supported by the German Research Foundation DFG (grant SI 1088/7-1). The work of P. T. Verronen is supported by the Academy of Finland (project No. 335555 ICT-SUNVAC). The development of AISstom has been supported by the German Science Foundation (DFG; grant no. WI4417/2-1). J.M. Wissing is supported by the German Aerospace Center (DLR; grant no. D/921/67284894).

M. Sinnhuber, M. A. Clilverd, B. Funke, C. E. Randall, C. J. Rodger, J. M. Wissing, and P. T. Verronen would like to thank the International Space Science Institute, Bern, Switzerland for supporting the project "Quantifying Hemispheric Differences in Particle Forcing Effects on Stratospheric Ozone" (Leader: D. R. Marsh).

The NOAA/POES data used in this study are available from the National Oceanic and Atmospheric Administration (`https://www.ngdc.noaa.gov/stp/satellite/poes/dataaccess.html`). The solar wind parameters and geomagnetic indices are obtained from the NASA OMNIWeb (`http://cdaweb.gsfc.nasa.gov`). Furthermore, the AIMOS and AISstorm ionization rate are available at https://aimos.physik.uos.de/, and the ApEEP ionization rates are available at https://solarisheppa.geomar.de/cmip6. This paper uses data from the Heliospheric Shock Database, generated and maintained at the University of Helsinki (`http://ipshocks.fi`). The hourly solar wind structure list was provided by Ian Richardson of the University of Maryland and NASA Goddard Space Flight Center via the CEDAR Database at the National Center for Atmospheric Research, which is supported by the National Science Foundation (`http://cedarweb.vsp.ucar.edu/wiki/index.php/Tools_and_Models:Solar_Wind_Structures`). The Whole Atmosphere Community Climate Model are freely available and can be used by the community (`http://www.cesm.ucar.edu/`).

References

Agostinelli, S., Allison, J., Amako, K., Apostolakis, J., Araujo, H., Arce, P., ... Zschiesche, D. (2003). Geant4—a simulation toolkit. *Nuclear Instruments and Methods in Physics Research Section A: Accelerators, Spectrometers, Detectors and Associated Equipment*, *506*(3), 250 - 303. Retrieved from `http://www.sciencedirect.com/science/article/pii/S0168900203013688` doi: https://doi.org/10.1016/S0168-9002(03)01368-8

Andersson, M. E., Verronen, P. T., Marsh, D. R., Päivärinta, S.-M., & Plane, J. M. C. (2016). WACCM-D – Improved modeling of nitric acid and active chlorine during energetic particle precipitation. *Journal of Geophysical*

Research: Atmospheres, *121*, 10,328–10,341. doi: 10.1002/2015JD024173

Andersson, M. E., Verronen, P. T., Marsh, D. R., Seppälä, A., Päivärinta, S.-M., Rodger, C. J., ... van de Kamp, M. (2018). Polar ozone response to energetic particle precipitation over decadal time scales: The role of medium-energy electrons. *Journal of Geophysical Research: Atmospheres*, *123*, 607–622. doi: 10.1002/2017JD027605

Andersson, M. E., Verronen, P. T., Wang, S., Rodger, C. J., Clilverd, M. A., & Carson, B. R. (2012). Precipitating radiation belt electrons and enhancements of mesospheric hydroxyl during 2004–2009. *Journal of Geophysical Research: Atmospheres*, *117*(D9). Retrieved from `https://agupubs.onlinelibrary.wiley.com/doi/abs/10.1029/2011JD017246` doi: 10.1029/2011JD017246

Arsenovic, P., Damiani, A., Rozanov, E., Funke, B., Stenke, A., & Peter, T. (2019). Reactive nitrogen (NO_y) and ozone responses to energetic electron precipitation during southern hemisphere winter. *Atmospheric Chemistry and Physics*, *19*(14), 9485–9494. Retrieved from `https://acp.copernicus.org/articles/19/9485/2019/` doi: 10.5194/acp-19-9485-2019

Asikainen, T. (2017). Calibrated and corrected POES/MEPED energetic particle observations. In A., Belehaki, M. Hapgood and J. Watermann (Ed.), *The espas e-infrastructure: Access to data in near-earth space* (p. 57-69). London, UK: EDP Open. doi: 10.1051/978-2-7598-1949-2

Asikainen, T. (2019). New homogeneous composite of energetic electron fluxes from poes: 2. intercalibration of sem-1 and sem-2. *Journal of Geophysical Research: Space Physics*, *124*(7), 5761-5782. Retrieved from `https://agupubs.onlinelibrary.wiley.com/doi/abs/10.1029/2019JA026699` doi: 10.1029/2019JA026699

Asikainen, T., & Mursula, K. (2011). Recalibration of NOAA/MEPED energetic proton measurements. *J. Atmos. Solar-Terrestrial Phys.*, *73*, 335-347, doi:10.1016/j.jastp.2009.12.011.

Asikainen, T., & Mursula, K. (2013). Correcting the NOAA/MEPED energetic electron fluxes for detector efficiency and proton contamination. *J. Geophys. Res.*, *118*, 6500-6510. doi: 10.1002/jgra.50584

Asikainen, T., Mursula, K., & Maliniemi, V. (2012). Correction of detector noise and recalibration of NOAA/MEPED energetic proton fluxes. *J. Geophys. Res.*, *117*, A09204, doi:10.1029/2012JA017593.

Asikainen, T., & Ruopsa, M. (2016). Solar wind drivers of energetic electron precipitation. *Journal of Geophysical Research: Space Physics*, *121*(3), 2209-2225. Retrieved from `https://agupubs.onlinelibrary.wiley.com/doi/abs/10.1002/2015JA022215` doi: 10.1002/2015JA022215

Asikainen, T., & Ruopsa, M. (2019). New homogeneous composite of energetic electron fluxes from poes satellites: 1. correction for background noise and orbital drift. *Journal of Geophysical Research: Space Physics*, *124*(2), 1203-1221. Retrieved from `https://agupubs.onlinelibrary.wiley.com/doi/abs/10.1029/2018JA026214` doi: 10.1029/2018JA026214

Bailey, S. M., Thurairajah, B., Randall, C. E., Holt, L., Siskind, D. E., Harvey, V. L., ... Russell III, J. M. (2014). A multi tracer analysis of thermosphere to stratosphere descent triggered by the 2013 stratospheric sudden warming. *Geophysical Research Letters*, *41*(14), 5216-5222. Retrieved from `https://agupubs.onlinelibrary.wiley.com/doi/abs/10.1002/2014GL059860` doi: https://doi.org/10.1002/2014GL059860

Bender, S., Sinnhuber, M., Espy, P., & Burrows, J. (2019). Mesospheric nitric oxide model from SCIAMACHY data. *Atmos. Chem. Phys.*, *19*, 2135–2147. doi: 10.5194/acp-19-2135-2019

Carson, B. R., Rodger, C. J., & Clilverd, M. A. (2013). Poes satellite observations of emic-wave driven relativistic electron precipitation during 1998–2010.

Journal of Geophysical Research: Space Physics, *118*(1), 232-243. Retrieved from https://agupubs.onlinelibrary.wiley.com/doi/abs/10.1029/2012JA017998 doi: 10.1029/2012JA017998

Clilverd, M. A., Rodger, C. J., van de Kamp, M., & Verronen, P. T. (2020). Electron precipitation from the outer radiation belt during the st. patrick's day storm 2015: Observations, modeling, and validation. *Journal of Geophysical Research: Space Physics*, *125*(2). Retrieved from https://agupubs.onlinelibrary.wiley.com/doi/10.1029/2019JA027725 doi: doi.org/10.1029/2019JA027725

Crutzen, P. J., Isaksen, I. S. A., & Reid, G. C. (1975). Solar proton events: Stratospheric sources of nitric oxide. *Science*, *189*(4201), 457–459. Retrieved from https://science.sciencemag.org/content/189/4201/457 doi: 10.1126/science.189.4201.457

Crutzen, P. J., & Solomon, S. (1980). Response of mesopheric ozone to particle precipitation. *Planetary and Space Science*, *28*(12), 1147 - 1153. Retrieved from http://www.sciencedirect.com/science/article/pii/0032063380900732 doi: https://doi.org/10.1016/0032-0633(80)90073-2

Evans, D. S., & Greer, M. S. (2004). Polar orbiting environmental satellite space environment monitor - 2: Instrument descriptions and archive data documentation. *NOAA Technical Memorandum, Boulder, Colorado OAR SEC 93, 93, version 1.4*.

Fang, X., Randall, C. E., Lummerzheim, D., Solomon, S. C., Mills, M. J., Marsh, D. R., … Lu, G. (2008). Electron impact ionization: A new parameterization for 100 ev to 1 mev electrons. *Journal of Geophysical Research: Space Physics*, *113*(A9). Retrieved from https://agupubs.onlinelibrary.wiley.com/doi/abs/10.1029/2008JA013384 doi: 10.1029/2008JA013384

Fang, X., Randall, C. E., Lummerzheim, D., Wang, W., Lu, G., Solomon, S. C., & Frahm, R. A. (2010). Parameterization of monoenergetic electron impact ionization. *Geophysical Research Letters*, *37*(22). Retrieved from https://agupubs.onlinelibrary.wiley.com/doi/abs/10.1029/2010GL045406 doi: 10.1029/2010GL045406

Funke, B., Ball, W., Bender, S., Gardini, A., Harvey, L. V., Lambert, A., … Yushkov, V. (2017). Heppa-ii model–measurement intercomparison project: Epp indirect effects during the dynamically perturbed nh winter 2008–2009. *Atmos. Chem. Phys.*, *17*. doi: 10.5194/acp-17-3573-2017

Funke, B., Baumgaertner, A., Calisto, M., Egorova, T., Jackman, C. H., Kieser, J., … Wissing, J. M. (2011). Composition changes after the "halloween" solar proton event: the high energy particle precipitation in the atmosphere (heppa) model versus mipas data intercomparison study. *Atmospheric Chemistry and Physics*, *11*(17), 9089–9139. Retrieved from https://acp.copernicus.org/articles/11/9089/2011/ doi: 10.5194/acp-11-9089-2011

Funke, B., López-Puertas, M., Stiller, G. P., & von Clarmann, T. (2014). Mesospheric and stratospheric noy produced by energetic particle precipitation during 2002–2012. *Journal of Geophysical Research: Atmospheres*, *119*(7), 4429-4446. Retrieved from https://agupubs.onlinelibrary.wiley.com/doi/abs/10.1002/2013JD021404 doi: 10.1002/2013JD021404

Galand, M., & Evans, D. S. (2000). Radiation damage of the proton meped detector on poes (tiros/noaa) satellites. *NOAA Technical Memorandum, Boulder, Colorado OAR 456-SEC. 42*.

Gettelman, A., Mills, M. J., Kinnison, R. R., D. E.and Garcia, Smith, A. K., Marsh, D. R., Tilmes, S., … Randel, W. J. (2019). The whole atmosphere community climate model version 6 (WACCM6). *J. Geophys. Res. Atmos.*, *124*, 12380–12403. doi: 10.1029/2019JD030943

Häkkilä, T., Verronen, P. T., Millán, L., Szelag, M. E., Kalakoski, N., & Kero, A. (2020). Odd hydrogen response thresholds for indication of solar proton and electron impact in the mesosphere and stratosphere. *Annales Geophysicae*, *38*(6), 1299–1312. Retrieved from https://angeo.copernicus.org/articles/38/1299/2020/ doi: 10.5194/angeo-38-1299-2020

Hardman, R., Clilverd, M. A., Rodger, C. J., Brundell, J. B., Duthie, R., Holzworth, R. H., ... Macusova, E. (2015). A case study of electron precipitation fluxes due to plasmaspheric hiss. *Journal of Geophysical Research: Space Physics*, *120*(8), 6736-6748. Retrieved from https://agupubs.onlinelibrary.wiley.com/doi/abs/10.1002/2015JA021429 doi: 10.1002/2015JA021429

Hendrickx, K., Megner, L., Gumbel, J., Siskind, D. E., Orsolini, Y. J., Tyssøy, H. N., & Hervig, M. (2015). Observation of 27 day solar cycles in the production and mesospheric descent of epp-produced no. *Journal of Geophysical Research: Space Physics*, *120*(10), 8978-8988. Retrieved from https://agupubs.onlinelibrary.wiley.com/doi/abs/10.1002/2015JA021441 doi: 10.1002/2015JA021441

Hendrickx, K., Megner, L., Marsh, D. R., & Smith-Johnsen, C. (2018). Production and transport mechanisms of no in the polar upper mesosphere and lower thermosphere in observations and models. *Atmospheric Chemistry and Physics*, *18*(12), 9075–9089. Retrieved from https://acp.copernicus.org/articles/18/9075/2018/ doi: 10.5194/acp-18-9075-2018

Hurrell, J. W., Holland, M. M., Gent, P. R., Ghan, S., Kay, J. E., Kushner, P. J., ... Marshall, S. (2013, 09). The Community Earth System Model: A Framework for Collaborative Research. *Bulletin of the American Meteorological Society*, *94*(9), 1339-1360. Retrieved from https://doi.org/10.1175/BAMS-D-12-00121.1 doi: 10.1175/BAMS-D-12-00121.1

Jackman, C. H., DeLand, M. T., Labow, G. J., Fleming, E. L., Weisenstein, D. K., Ko, M. K. W., ... Russell, J. M. (2005). Neutral atmospheric influences of the solar proton events in october–november 2003. *Journal of Geophysical Research: Space Physics*, *110*(A9). Retrieved from https://agupubs.onlinelibrary.wiley.com/doi/abs/10.1029/2004JA010888 doi: 10.1029/2004JA010888

Kavanagh, A. J., Cobbett, N., & Kirsch, P. (2018). Radiation belt slot region filling events: Sustained energetic precipitation into the mesosphere. *Journal of Geophysical Research: Space Physics*, *123*(9), 7999-8020. Retrieved from https://agupubs.onlinelibrary.wiley.com/doi/abs/10.1029/2018JA025890 doi: 10.1029/2018JA025890

Kennel, C. F., & Petschek, H. E. (1966). Limit on stably trapped particle fluxes. *Journal of Geophysical Research (1896-1977)*, *71*(1), 1-28. Retrieved from https://agupubs.onlinelibrary.wiley.com/doi/abs/10.1029/JZ071i001p00001 doi: 10.1029/JZ071i001p00001

Kilpua, E. K. J., Lumme, E., Andreeova, K., Isavnin, A., & Koskinen, H. E. J. (2015). Properties and drivers of fast interplanetary shocks near the orbit of the earth (1995–2013). *Journal of Geophysical Research: Space Physics*, *120*(6), 4112-4125. Retrieved from https://agupubs.onlinelibrary.wiley.com/doi/abs/10.1002/2015JA021138 doi: 10.1002/2015JA021138

Lam, M. M., Horne, R. B., Meredith, N. P., Glauert, S. A., Moffat-Griffin, T., & Green, J. C. (2010). Origin of energetic electron precipitation ¿30 kev into the atmosphere. *Journal of Geophysical Research: Space Physics*, *115*(A4). Retrieved from https://agupubs.onlinelibrary.wiley.com/doi/abs/10.1029/2009JA014619 doi: 10.1029/2009JA014619

Loewe, C. A., & Prölss, G. W. (1997). Classification and mean behavior of magnetic storms. *Journal of Geophysical Research: Space Physics*, *102*(A7), 14209-14213. Retrieved from https://agupubs.onlinelibrary.wiley.com/doi/abs/10.1029/96JA04020 doi: 10.1029/96JA04020

Marsh, D., Solomon, S., & Reynolds, A. (2004). Empirical model of nitric oxide in the lower thermosphere. *J. Geophys. Res.*, *109*. doi: 10.1029/2004JA010199

Matthes, K., Funke, B., Anderson, M., Barnard, L., Beer, J., Charbonneau, P., ... Versick, S. (2017). Solar forcing for cmip-6. *Geosci. Model. Dev.*, *10*, 2247-2302. doi: 10.5194/gmd-10-2247-2017

McIlwain, C. E. (1961). Coordinates for mapping the distribution of magnetically trapped particles. *J. Geophys. Res.*, *66*(11), 3681–3691. doi: 10.1029/JZ066i011p03681

Millan, R., McCarthy, M., & Sample, J. e. a. (2013). The balloon array for rbsp relativistic electron losses (barrel). *Space Sci Rev*, *179*, 503–530. doi: https://doi.org/10.1007/s11214-013-9971-z

Mironova, I. A., Artamonov, A. A., Bazilevskaya, G. A., Rozanov, E. V., Kovaltsov, G. A., Makhmutov, V. S., ... Karagodin, A. V. (2019). Ionization of the polar atmosphere by energetic electron precipitation retrieved from balloon measurements. *Geophysical Research Letters*, *46*(2), 990-996. Retrieved from `https://agupubs.onlinelibrary.wiley.com/doi/abs/10.1029/2018GL079421` doi: 10.1029/2018GL079421

Nesse Tyssøy, H., Haderlein, A., Sandanger, M., & Stadsnes, J. (2019). Intercomparison fo the POES/MEPED loss cone electron fluxes with the CMIP6 parametrization. *J. Geophys. Res.*, *124*, 628-642. doi: 10.1029/2018JA025745

Nesse Tyssøy, H., Sandanger, M. I., Ødegaard, L.-K. G., Stadsnes, J., Aasnes, A., & Zawedde, A. E. (2016). Energetic electron precipitation into the middle atmosphere—constructing the loss cone fluxes from meped poes. *Journal of Geophysical Research: Space Physics*, *121*(6), 5693-5707. Retrieved from `https://agupubs.onlinelibrary.wiley.com/doi/abs/10.1002/2016JA022752` doi: 10.1002/2016JA022752

Nesse Tyssøy, H., & Stadsnes, J. (2015). Cutoff latitude variation during solar proton events: Causes and consequences. *Journal of Geophysical Research: Space Physics*, *120*(1), 553-563. Retrieved from `https://agupubs.onlinelibrary.wiley.com/doi/abs/10.1002/2014JA020508` doi: 10.1002/2014JA020508

Newell, P. T., & Gjerloev, J. W. (2011). Evaluation of SuperMAG auroral electrojet indices as indicators of substorms and auroral power. *Journal of Geophysical Research (Space Physics)*, *116*(A15), A12211. doi: 10.1029/2011JA016779

Newnham, D. A., Clilverd, M. A., Rodger, C. J., Hendrickx, K., Megner, L., Kavanagh, A. J., ... Plane, J. M. C. (2018). Observations and modelling of increased nitric oxide in the Antarctic polar middle atmosphere associated with geomagnetic storm driven energetic electron precipitation. *J. Geophys. Res. Space*, *123*, 6009–6025. Retrieved from `https://doi.org/10.1029/2018JA025507` doi: 10.1029/2018JA025507

Ni, B., Bortnik, J., Thorne, R. M., Ma, Q., & Chen, L. (2013). Resonant scattering and resultant pitch angle evolution of relativistic electrons by plasmaspheric hiss. *Journal of Geophysical Research: Space Physics*, *118*(12), 7740-7751. Retrieved from `https://agupubs.onlinelibrary.wiley.com/doi/abs/10.1002/2013JA019260` doi: 10.1002/2013JA019260

O'Brien, T. P., & Moldwin, M. B. (2003). Empirical plasmapause models from magnetic indices. *Geophys. Res. Lett.*, *30*(4), 1152. doi: 10.1029/2002GL016007

Ødegaard, L.-K. G., Tyssøy, H. N., Sandanger, M. I. J., Stadsnes, J., & Søraas, F. (2016). Space weather impact on the degradation of noaa poes meped proton detectors. *J. Space Weather Space Clim.*, *6*, A26. Retrieved from `https://doi.org/10.1051/swsc/2016020` doi: 10.1051/swsc/2016020

Orsolini, Y. J., Smith-Johnsen, C., Marsh, D. R., Stordal, F., Rodger, C. J., Verronen, P. T., & Clilverd, M. A. (2018). Mesospheric nitric acid enhancements during energetic electron precipitation events simulated by waccm-d. *Journal of Geophysical Research: Atmospheres*, *123*(13), 6984-6998. Retrieved from `https://agupubs.onlinelibrary.wiley.com/doi/abs/10.1029/2017JD028211` doi: 10.1029/2017JD028211

Päivärinta, S.-M., Verronen, P. T., Funke, B., Gardini, A., Seppälä, A., & Andersson, M. E. (2016). Transport versus energetic particle precipitation: Northern polar stratospheric NO_x and ozone in January-March 2012. *Journal of Geophysical Research: Atmospheres*, *121*, 6085–6100. doi: 10.1002/2015JD024217

Peck, E. D. (2014). Impacts of energetic electron precipitation on the middle atmosphere. *Theses CU Boulder Atmospheric and Oceanic Sciences.*. Retrieved from `https://libraries.colorado.edu/search~S3?/i9781321498714/i9781321498714/-3,-1,0,E/frameset&FF=i9781321498714&1,1,?save=b8049740`

Peck, E. D., Randall, C. E., Green, J. C., Rodriguez, J. V., & Rodger, C. J. (2015). Poes meped differential flux retrievals and electron channel contamination correction. *Journal of Geophysical Research: Space Physics*, *120*(6), 4596-4612. Retrieved from `https://agupubs.onlinelibrary.wiley.com/doi/abs/10.1002/2014JA020817` doi: 10.1002/2014JA020817

Pérot, K., Urban, J., & Murtagh, D. P. (2014). Unusually strong nitric oxide descent in the arctic middle atmosphere in early 2013 as observed by odin/smr. *Atmospheric Chemistry and Physics*, *14*(15), 8009–8015. Retrieved from `https://acp.copernicus.org/articles/14/8009/2014/` doi: 10.5194/acp-14-8009-2014

Pettit, J. M., Randall, C. E., Peck, E. D., Marsh, D. R., van de Kamp, M., Fang, X., . . . Funke, B. (2019). Atmospheric effects of >30-keV energetic electron precipitation in the southern hemisphere winter during 2003. *Journal of Geophysical Research: Space Physics*, *124*(10), 8138-8153. Retrieved from `https://agupubs.onlinelibrary.wiley.com/doi/abs/10.1029/2019JA026868` doi: 10.1029/2019JA026868

Picone, J. M., Hedin, A. E., Drob, D. P., & Aikin, A. C. (2002). Nrlmsise-00 empirical model of the atmosphere: Statistical comparisons and scientific issues. *Journal of Geophysical Research: Space Physics*, *107*(A12), SIA 15-1-SIA 15-16. Retrieved from `https://agupubs.onlinelibrary.wiley.com/doi/abs/10.1029/2002JA009430` doi: 10.1029/2002JA009430

Randall, C. E., Harvey, V. L., Manney, G. L., Orsolini, Y., Codrescu, M., Sioris, C., . . . Russell III, J. M. (2005). Stratospheric effects of energetic particle precipitation in 2003–2004. *Geophysical Research Letters*, *32*(5). Retrieved from `https://agupubs.onlinelibrary.wiley.com/doi/abs/10.1029/2004GL022003` doi: 10.1029/2004GL022003

Randall, C. E., Harvey, V. L., Singleton, C. S., Bailey, S. M., Bernath, P. F., Codrescu, M., . . . Russell III, J. M. (2007). Energetic particle precipitation effects on the southern hemisphere stratosphere in 1992–2005. *Journal of Geophysical Research: Atmospheres*, *112*(D8). Retrieved from `https://agupubs.onlinelibrary.wiley.com/doi/abs/10.1029/2006JD007696` doi: 10.1029/2006JD007696

Rees, M. H. (1989). *Physics and chemistry of the upper atmospherephysics and chemistry of the upper atmosphere.* Cambridge [Cambridgeshire] ;: Cambridge University Press,.

Richardson, I. G., & Cane, H. V. (2012). Near-earth solar wind flows and related geomagnetic activity during more than four solar cycles (1963-2011). *J. Space Weather Space Clim.*, *2*, A02. Retrieved from `https://doi.org/10.1051/swsc/2012003` doi: 10.1051/swsc/2012003

Richmond, A. D. (1995). Ionospheric electrodynamics using magnetic apex coordinates. *Journal of geomagnetism and geoelectricity*, *47*(2), 191-212. doi: 10.5636/jgg.47.191

Rodger, C., Carson, B., Cummer, S., Gamble, R., Clilverd, M., Green, J., . . . Berthelier, J.-J. (2010a). Contrasting the efficiency of radiation belt losses caused by ducted and nonducted whistler-mode waves from ground-based transmitters. *Journal of Geophysical Research: Space Physics*, *115*(A12).

Retrieved from https://agupubs.onlinelibrary.wiley.com/doi/abs/10.1029/2010JA015880 doi: 10.1029/2010JA015880

Rodger, C., Clilverd, M., Green, J., & Lam, M. (2010b). Use of POES SEM-2 observations to examine radiation belt dynamics and energetic electron precipitation into the atmosphere. *J. Geophys. Res.*, *115*. doi: 10.1029/2008JA014023

Rodger, C., Kavanagh, A. J., Clilverd, M. A., & Marple, S. R. (2013). Comparison between poes energetic electron precipitation observations and riometer absorptions: Implications for determining true precipitation fluxes. *Journal of Geophysical Research: Space Physics*, *118*(12), 7810-7821. Retrieved from https://agupubs.onlinelibrary.wiley.com/doi/abs/10.1002/2013JA019439 doi: 10.1002/2013JA019439

Rodger, C. J., Enell, C. F., Turunen, E., Clilverd, M. A., Thomson, N. R., & Verronen, P. T. (2007, August). Lightning-driven inner radiation belt energy deposition into the atmosphere: implications for ionisation-levels and neutral chemistry. *Annales Geophysicae*, *25*(8), 1745-1757. doi: 10.5194/angeo-25-1745-2007

Sandanger, M. I., Ødegaard, L.-K. G., Nesse Tyssøy, H., Stadsnes, J., Søraas, F., Oksavik, K., & Aarsnes, K. (2015). In-flight calibration of noaa poes proton detectors—derivation of the meped correction factors. *Journal of Geophysical Research: Space Physics*, *120*(11), 9578-9593. Retrieved from https://agupubs.onlinelibrary.wiley.com/doi/abs/10.1002/2015JA021388 doi: 10.1002/2015JA021388

Schmidt, H., Brasseur, G. P., Charron, M., Manzini, E., Giorgetta, M. A., Diehl, T., … Walters, S. (2006, Jan). The HAMMONIA Chemistry Climate Model: Sensitivity of the Mesopause Region to the 11-Year Solar Cycle and CO2 Doubling. *Journal of Climate*, *19*(16), 3903. doi: 10.1175/JCLI3829.1

Sinnhuber, M., Berger, U., Funke, B., Nieder, H., Reddmann, T., Stiller, G., … Wissing, J. (2018). Noy production, ozone loss and changes in net radiative heating due to energetic particle precipitation in 2002-2010. *Atmos. Chem. Phys.*, *18*, 1115-1147. doi: 10.5194/acp-18-1115-2018

Sinnhuber, M., Friederich, F., Bender, S., & Burrows, J. P. (2016). The response of mesospheric no to geomagnetic forcing in 2002–2012 as seen by sciamachy. *J. Geophys. Res.*, *121*, 3603–3620. doi: 10.1002/2015JA022284

Sinnhuber, M., Kazeminejad, S., & Wissing, J. M. (2011). Interannual variation of nox from the lower thermosphere to the upper stratosphere in the years 1991–2005. *Journal of Geophysical Research: Space Physics*, *116*(A2). Retrieved from https://agupubs.onlinelibrary.wiley.com/doi/abs/10.1029/2010JA015825 doi: 10.1029/2010JA015825

Sinnhuber, M., Nesse Tyssoy, H., Asikainen, T., Bender, S., Funke, B., Hendrickx, K., … Yakovchuk, O. (2021). Heppa iii intercomparison experiment on1medium-energy electrons, part ii: Model-measurement intercomparison of nitric oxide (no) during a geomagnetic storm in april 2010. *J. Geophys. Rev.*, *in review*.

Sinnhuber, M., Nieder, H., & Wieters, N. (2012). Energetic particle precipitation and the chemistry of the mesosphere/lower thermosphere. *Surv. Geophys.*, *33*, 1281–1334. doi: 10.1007/s10712-012-9201-3

Smith-Johnsen, C., Marsh, D., Orsolini, Y., Nesse Tyssøy, H., Hendrickx, K., Sandanger, M., … Stordal, F. (2018). Nitric oxide response to the april 2010 electron precipitation event: Using waccm and waccm-d with and without medium-energy electrons. *J. Geophys. Res.*, *123*, 5232–5245. doi: 10.1029/2018JA025418

Smith-Johnsen, C., Nesse Tyssøy, H., Hendrickx, K., Orsolini, Y., Kumar, G., Glesnes Ødegard, L.-K., … Megner, L. (2017). Direct and indirect electron precipitation effect on nitric oxide in the polar middle atmosphere using a full-range energy spectrum. *J. Geophys. Res. Space Physics*, *122*, 8679–8693.

doi: 10.1002/2017JA024364

Solomon, S. (2001). Auroral particle transport using monte carlo and hybrid methods. *Journal of Geophysical Research: Space Physics*, *106*(A1), 107-116. Retrieved from https://agupubs.onlinelibrary.wiley.com/doi/abs/10.1029/2000JA002011 doi: 10.1029/2000JA002011

Solomon, S., Rusch, D., Gérard, J., Reid, G., & Crutzen, P. (1981). The effect of particle precipitation events on the neutral and ion chemistry of the middle atmosphere: Ii. odd hydrogen. *Planetary and Space Science*, *29*(8), 885 - 893. doi: https://doi.org/10.1016/0032-0633(81)90078-7

Summers, D., Ni, B., & Meredith, N. P. (2007). Timescales for radiation belt electron acceleration and loss due to resonant wave-particle interactions: 2. evaluation for vlf chorus, elf hiss, and electromagnetic ion cyclotron waves. *Journal of Geophysical Research: Space Physics*, *112*(A4). Retrieved from https://agupubs.onlinelibrary.wiley.com/doi/abs/10.1029/2006JA011993 doi: 10.1029/2006JA011993

Swider, W., & Keneshea, T. (1973). Decrease of ozone and atomic oxygen in the lower mesosphere during a pca event. *Planetary and Space Science*, *21*(11), 1969 - 1973. Retrieved from http://www.sciencedirect.com/science/article/pii/0032063373901268 doi: https://doi.org/10.1016/0032-0633(73)90126-8

Sætre, C., Stadsnes, J., Nesse, H., Aksnes, A., Petrinec, S. M., Barth, C. A., ... Østgaard, N. (2004). Energetic electron precipitation and the no abundance in the upper atmosphere: A direct comparison during a geomagnetic storm. *Journal of Geophysical Research: Space Physics*, *109*(A9). Retrieved from https://agupubs.onlinelibrary.wiley.com/doi/abs/10.1029/2004JA010485 doi: 10.1029/2004JA010485

Turunen, E., Verronen, P. T., Seppälä, A., Rodger, C. J., Clilverd, M. A., Tamminen, J., ... Ulich, T. (2009). Impact of different energies of precipitating particles on nox generation in the middle and upper atmosphere during geomagnetic storms. *Journal of Atmospheric and Solar-Terrestrial Physics*, *71*(10), 1176 - 1189. Retrieved from http://www.sciencedirect.com/science/article/pii/S1364682608001958 (High Speed Solar Wind Streams and Geospace Interactions) doi: https://doi.org/10.1016/j.jastp.2008.07.005

van de Kamp, M., Rodger, C. J., Seppälä, A., Clilverd, M. A., & Verronen, P. T. (2018). An updated model providing long-term data sets of energetic electron precipitation, including zonal dependence. *J. Geophys. Res. Atmos.*, *123*. doi: 10.1029/2017JD028253

van de Kamp, M., Seppälä, A., Clilverd, M. A., Rodger, C. J., Verronen, P. T., & Whittaker, I. C. (2016). A model providing long-term data sets of energetic electron precipitation during geomagnetic storms. *J. Geophys. Res. Atmos.*, *121*. doi: 10.1002/2015JD024212

Verronen, P. T., Andersson, M. E., Marsh, D. R., Kovács, T., & Plane, J. M. C. (2016). Waccm-d—whole atmosphere community climate model with d-region ion chemistr. *Journal of Advances in Modeling Earth Systems*, *8*, 954– 975. Retrieved from https://agupubs.onlinelibrary.wiley.com/doi/full/10.1002/2015MS000592 doi: 10.1002/2015MS000592

Verronen, P. T., & Lehmann, R. (2013). Analysis and parameterisation of ionic reactions affecting middle atmospheric HO_x and NO_y during solar proton events. *Ann. Geophys.*, *31*, 909–956. doi: 10.5194/angeo-31-909-2013

Verronen, P. T., Rodger, C. J., Clilverd, M. A., & Wang, S. (2011). First evidence of mesospheric hydroxyl response to electron precipitation from the radiation belts. *Journal of Geophysical Research: Atmospheres*, *116*, D07307. doi: 10.1029/2010JD014965

Verronen, P. T., Seppälä, A., Kyrölä, E., Tamminen, J., Pickett, H. M., & Turunen, E. (2006). Production of odd hydrogen in the mesosphere during the january

2005 solar proton event. *Geophysical Research Letters*, *33*(24). Retrieved from `https://agupubs.onlinelibrary.wiley.com/doi/abs/10.1029/2006GL028115` doi: 10.1029/2006GL028115

Voss, H. D., Walt, M., Imhof, W. L., Mobilia, J., & Inan, U. S. (1998). Satellite observations of lightning-induced electron precipitation. *Journal of Geophysical Research: Space Physics*, *103*(A6), 11725-11744. Retrieved from `https://agupubs.onlinelibrary.wiley.com/doi/abs/10.1029/97JA02878` doi: 10.1029/97JA02878

Weeks, L. H., Cuikay, R. S., & Corbin, J. R. (1972, 09). Ozone Measurements in the Mesosphere During The Solar Proton Event of 2 November 1969. *Journal of the Atmospheric Sciences*, *29*(6), 1138-1142. Retrieved from `https://doi.org/10.1175/1520-0469(1972)029<1138:OMITMD>2.0.CO;2` doi: 10.1175/1520-0469(1972)029⟨1138:OMITMD⟩2.0.CO;2

Whittaker, I. C., Clilverd, M. A., & Rodger, C. J. (2014). Characteristics of precipitating energetic electron fluxes relative to the plasmapause during geomagnetic storms. *Journal of Geophysical Research: Space Physics*, *119*(11), 8784-8800. Retrieved from `https://agupubs.onlinelibrary.wiley.com/doi/abs/10.1002/2014JA020446` doi: 10.1002/2014JA020446

Whittaker, I. C., Gamble, R. J., Rodger, C. J., Clilverd, M. A., & Sauvaud, J.-A. (2013). Determining the spectra of radiation belt electron losses: Fitting demeter electron flux observations for typical and storm times. *J. Geophys. Res. Space Physics*, *118*, 7611–7623. doi: 10.1002/2013JA019228

Whittaker, I. C., Rodger, C. J., Clilverd, M. A., & Sauvaud, J.-A. (2014). The effects and correction of the geometric factor for the poes/meped electron flux instrument using a multisatellite comparison. *J. Geophys. Res. Space Physics*, *119*, 6386–6404. doi: 10.1002/2014JA020021

Wissing, J. M., & Kallenrode, M.-B. (2009). Atmospheric ionization module osnabrück (aimos): A 3-d model to determine atmospheric ionization by energetic charged particles from different populations. *Journal of Geophysical Research: Space Physics*, *114*(A6). Retrieved from `https://agupubs.onlinelibrary.wiley.com/doi/abs/10.1029/2008JA013884` doi: 10.1029/2008JA013884

Yando, K., Millan, R. M., Green, J. C., & Evans, D. S. (2011). A monte carlo simulation of the noaa poes medium energy proton and electron detector instrument. *Journal of Geophysical Research: Space Physics*, *116*(A10). Retrieved from `https://agupubs.onlinelibrary.wiley.com/doi/abs/10.1029/2011JA016671` doi: 10.1029/2011JA016671

Zawedde, A. E., Nesse Tyssøy, H., Hibbins, R., Espy, P. J., Ødegaard, L.-K. G., Sandanger, M. I., & Stadsnes, J. (2016). The impact of energetic electron precipitation on mesospheric hydroxyl during a year of solar minimum. *Journal of Geophysical Research: Space Physics*, *121*(6), 5914-5929. Retrieved from `https://agupubs.onlinelibrary.wiley.com/doi/abs/10.1002/2016JA022371` doi: 10.1002/2016JA022371

Zawedde, A. E., Nesse Tyssøy, H., Stadsnes, J., & Sandanger, M. I. (2018). The impact of energetic particle precipitation on mesospheric oh – variability of the sources and the background atmosphere. *Journal of Geophysical Research: Space Physics*, *123*(7), 5764-5789. Retrieved from `https://agupubs.onlinelibrary.wiley.com/doi/abs/10.1029/2017JA025038` doi: https://doi.org/10.1029/2017JA025038

Ødegaard, L.-K. G., Tyssøy, H. N., Søraas, F., Stadsnes, J., & Sandanger, M. I. (2017). Energetic electron precipitation in weak to moderate corotating interaction region-driven storms. *Journal of Geophysical Research: Space Physics*, *122*(3), 2900-2921. Retrieved from `https://agupubs.onlinelibrary.wiley.com/doi/abs/10.1002/2016JA023096` doi: 10.1002/2016JA023096